A study on heterogeneous trench-assisted single-mode multi-core fiber and few-mode multi-core fiber

Jiajing Tu

Division of Media and Network Technologies

Graduate School of Information Science and Technology

Hokkaido University

Table of Content

Chapter 1 Introduction

For the last twenty years, the optical communication technologies have seen an increase in transmission capacity per fiber by three orders of magnitudes, achieving several Tbit/s transmissions. If the data traffic continues to increase with 40 % ~ 70 % per year, a capacity increase by three or five orders of magnitudes should be anticipated for the next twenty years. This means that in twenty years, the backbone transmission capacity should support well over Pbit/s per fiber and the core network should support Ebit/s throughput where at home, Tbit/s access handling 3D super-high definition videos will be a reality [1]. There are three kinds of "multi-" (3M) technologies to achieve extremely large transmission capacity and throughput, which are "multi-mode control", "multi-core fiber", and "multi-level modulation". They were proposed by the collaborative study group "EXAT (**EX**tremely **A**dvanced **T**ransmission)" in Japan [2].

Therefore, how to cope with the exponentially increasing demand for transmission capacity per fiber is a hot topic nowadays. At present, several multiplexing technologies such as space-division multiplexing (SDM) using multi-core fiber (MCF) [3, 4] and mode-division multiplexing (MDM) using few-mode fiber (FMF) [5, 6] are being intensively investigated to solve the above-related issue in the current conventional optical communication systems. For MCF, 305-Tb/s SDM transmission using a 19-core fiber has been reported [7] and 1.01-Pb/s SDM transmission using a 12-core fiber has also been proposed [8]. For FMF, the fabrication of a 4-mode fiber that exhibits low bend losses, low mode coupling and low inter- and intra-mode nonlinear effects has been reported [9]. Furthermore, differential mode delay managed transmission lines for wide-band WDM-MIMO system have also been reported [10, 11]. Recently, the combination of multi-core and few-mode design has been presented to further increase the capacity of fiber [12, 13].

In this study, we propose a sort of heterogeneous trench-assisted MCF (Hetero-TA-MCF) to obtain much lower crosstalk, in which there are not only identical cores but also non-identical cores and the cores are more closely packed in a definite space. What's more, two non-identical cores deployed in the fiber are not only to decrease the crosstalk but also to make the fiber insensitive to the bending extent [14]. The trench layer is deployed around each core to realize lower inter-core crosstalk even with small core pitch [15]. After adjusting the location and thickness of trench layer, we can find a relative optimum design scheme for the Hetero-TA-MCF. Besides the MCF, we also design a kind of Hetero-TA-FM-MCF with low differential mode delay (DMD) and large effective area (A_{eff}). After analyzing the

relationship among the parameters of profile, we can propose the optimum scheme for Hetero-TA-FM-MCF too. In addition, to evaluate a superior MCF or FMF, the discussion of inter-core crosstalk under bent condition is also an important aspect during the design process. Therefore, how to calculate the inter-core crosstalk for bent MCF and FMF by using an analytical method is a big issue.

This thesis is structured as follows.

In chapter 2, we introduce the derivation of mode-coupling coefficient (MCC) based on perturbation theory, and then calculate the MCC between two adjacent trench-assisted cores by using analytical method and finite element method [16]. Additionally, we also introduce a special approach for the MCC calculation between two identical cores based on mode interference.

In chapter 3, we introduce the calculation method for inter-core crosstalk in the bent fiber based on coupled-mode theory and coupled-power theory.

In chapter 4, we describe and explain the design methods for the cores, trench layers and core number in multi-core fibers (MCFs) in detail through analyzing the characteristics of the heterogeneous trench-assisted multi-core fiber (Hetero-TA-MCF). According to such method, we propose relative optimal design schemes for such Hetero-TA-MCF, inside which cores are arranged in one-ring structure. This Hetero-TA-MCF is a kind of bend-insensitive MCF with high density of cores and ultra-low crosstalk.

In chapter 5, we propose a kind of heterogeneous multi-core fiber (Hetero-MCF) with trench-assisted multi-step index few-mode core (TA-MSI-FMC) deployed inside. After analyzing the impact of each parameter on differential mode delay (DMD), we design a couple of TA-MSI-FMCs with large A_{eff} for each mode and meanwhile make sure low DMD in each core over C+L bands. After analyzing how the position of trench structure affects the DMD and DMD slope for wavelength, we present a relative optimal design scheme for the Hetero-TA-MSI-FM-MCF. At last, we propose two kinds of strategies for the application of fiber.

In chapter 6, conclusions of this thesis are discribed.

Chapter 2 Calculation method for mode-coupling coefficient of optical fiber

2.1 Introduction

In axially uniform optical waveguides, a number of propagation modes exist. These propagation modes are specific to each waveguide and satisfy the orthogonality condition between the modes [17]. If two waveguides are brought close together as shown in Fig. 2.1, optical modes of each waveguide either couple or interfere with each other. When the electromagnetic field distributions after mode coupling do not differ substantially from those before coupling, the propagation characteristics of the coupled waveguides can be analyzed by the perturbation method [18]. On the other hand, the mode-coupling effect between two identical directional waveguides can also be analyzed by the interference phenomena between the even and odd modes.

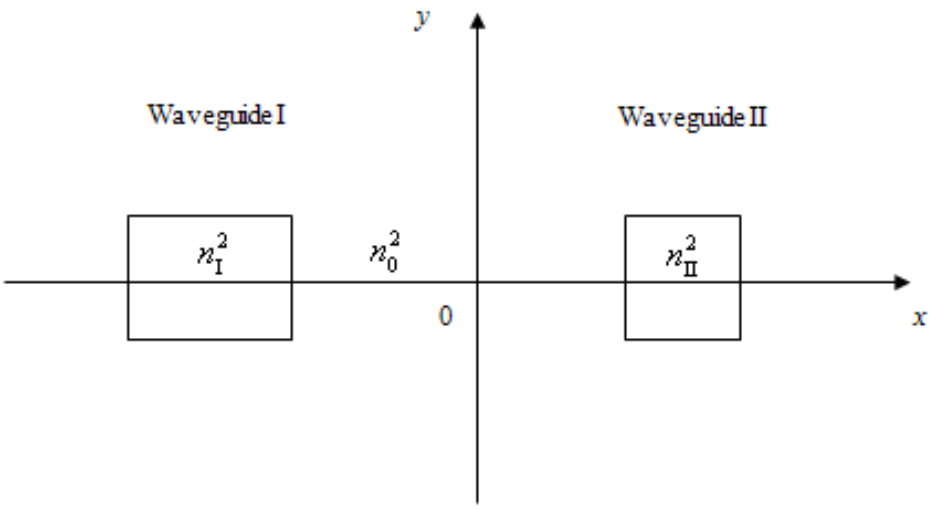

Fig. 2.1 Directionally coupled optical waveguides.

2.2 Derivation of mode-coupling coefficient based on perturbation theory

We define $\tilde{E}_p, \tilde{H}_p$ as the eigen modes in each optical waveguide before mode coupling,

and they satisfy the following Maxwell's equations [17]:

$$\begin{cases} \nabla \times \tilde{\boldsymbol{E}}_p = -j\omega\mu_0 \tilde{\boldsymbol{H}}_p \\ \nabla \times \tilde{\boldsymbol{H}}_p = j\omega\varepsilon_0 N_p^{\ 2} \tilde{\boldsymbol{E}}_p \end{cases}, \quad (p = 1, 2) \tag{2.1}$$

where $N_p(x, y)$ represents the refractive-index distribution of each waveguide, ω is an angular frequency of the sinusoidally varying electromagnetic fields, ε_0 is the permittivity of the medium, and μ_0 is the permeability of the medium. We assume that the electromagnetic fields of the coupled waveguide can be expressed as the sum of the eigen modes in each waveguides [17]:

$$\begin{cases} \tilde{\boldsymbol{E}} = A(z)\tilde{\boldsymbol{E}}_1 + B(z)\tilde{\boldsymbol{E}}_2 \\ \tilde{\boldsymbol{H}} = A(z)\tilde{\boldsymbol{H}}_1 + B(z)\tilde{\boldsymbol{H}}_2 \end{cases}. \tag{2.2}$$

The electromagnetic fields in the coupled waveguide $\tilde{E}$ and $\tilde{H}$ also should satisfy Maxwell's equations. Then we can substitute Eq. (2.2) into

$$\begin{cases} \nabla \times \tilde{\boldsymbol{E}} = -j\omega\mu_0 \tilde{\boldsymbol{H}} \\ \nabla \times \tilde{\boldsymbol{H}} = j\omega\varepsilon_0 N^2 \tilde{\boldsymbol{E}} \end{cases}, \tag{2.3}$$

and using Eq. (2.1) and the vector formula

$$\nabla \times (A\boldsymbol{E}) = A\nabla \times \boldsymbol{E} + \nabla A \times \boldsymbol{E} = A\nabla \times \boldsymbol{E} + \frac{dA}{dz} u_z \times \boldsymbol{E},$$

We obtain the following relations [17]:

$$\left(\boldsymbol{u}_z \times \tilde{\boldsymbol{E}}_1\right)\frac{dA}{dz} + \left(\boldsymbol{u}_z \times \tilde{\boldsymbol{E}}_2\right)\frac{dB}{dz} = 0, \tag{2.4}$$

$$\left(\boldsymbol{u}_z \times \tilde{\boldsymbol{H}}_1\right)\frac{dA}{dz} - j\omega\varepsilon_0\left(N^2 - N_1^2\right)A\tilde{\boldsymbol{E}}_1 + \left(\boldsymbol{u}_z \times \tilde{\boldsymbol{H}}_2\right)\frac{dB}{dz} - j\omega\varepsilon_0\left(N^2 - N_2^2\right)B\tilde{\boldsymbol{E}}_2 = 0. \tag{2.5}$$

Here, $N(x, y)$ denotes the refractive-index distribution in the entire coupled waveguide. Substituting Eqs. (2.4) and (2.5) into the following integral equations:

$$\int_{-\infty}^{\infty}\int_{-\infty}^{\infty}[\tilde{\boldsymbol{E}}_1^*\cdot(2.5)-\tilde{\boldsymbol{H}}_1^*\cdot(2.4)]dxdy=0, \tag{2.6}$$

$$\int_{-\infty}^{\infty}\int_{-\infty}^{\infty}[\tilde{\boldsymbol{E}}_2^*\cdot(2.5)-\tilde{\boldsymbol{H}}_2^*\cdot(2.4)]dxdy=0, \tag{2.7}$$

we obtain [17]

$$\begin{aligned}
&\frac{dA}{dz}+\frac{dB}{dz}\frac{\int_{-\infty}^{\infty}\int_{-\infty}^{\infty}\boldsymbol{u}_z\cdot(\tilde{\boldsymbol{E}}_1^*\times\tilde{\boldsymbol{H}}_2+\tilde{\boldsymbol{E}}_2\times\tilde{\boldsymbol{H}}_1^*)dxdy}{\int_{-\infty}^{\infty}\int_{-\infty}^{\infty}\boldsymbol{u}_z\cdot(\tilde{\boldsymbol{E}}_1^*\times\tilde{\boldsymbol{H}}_1+\tilde{\boldsymbol{E}}_1\times\tilde{\boldsymbol{H}}_1^*)dxdy}\\
&+jA\frac{\omega\varepsilon_0\int_{-\infty}^{\infty}\int_{-\infty}^{\infty}(N^2-N_1^2)\tilde{\boldsymbol{E}}_1^*\cdot\tilde{\boldsymbol{E}}_1\,dxdy}{\int_{-\infty}^{\infty}\int_{-\infty}^{\infty}\boldsymbol{u}_z\cdot(\tilde{\boldsymbol{E}}_1^*\times\tilde{\boldsymbol{H}}_1+\tilde{\boldsymbol{E}}_1\times\tilde{\boldsymbol{H}}_1^*)dxdy}\\
&+jB\frac{\omega\varepsilon_0\int_{-\infty}^{\infty}\int_{-\infty}^{\infty}(N^2-N_2^2)\tilde{\boldsymbol{E}}_1^*\cdot\tilde{\boldsymbol{E}}_2\,dxdy}{\int_{-\infty}^{\infty}\int_{-\infty}^{\infty}\boldsymbol{u}_z\cdot(\tilde{\boldsymbol{E}}_1^*\times\tilde{\boldsymbol{H}}_1+\tilde{\boldsymbol{E}}_1\times\tilde{\boldsymbol{H}}_1^*)dxdy}=0,
\end{aligned} \tag{2.8}$$

$$\begin{aligned}
&\frac{dB}{dz}+\frac{dA}{dz}\frac{\int_{-\infty}^{\infty}\int_{-\infty}^{\infty}\boldsymbol{u}_z\cdot(\tilde{\boldsymbol{E}}_2^*\times\tilde{\boldsymbol{H}}_1+\tilde{\boldsymbol{E}}_1\times\tilde{\boldsymbol{H}}_2^*)dxdy}{\int_{-\infty}^{\infty}\int_{-\infty}^{\infty}\boldsymbol{u}_z\cdot(\tilde{\boldsymbol{E}}_2^*\times\tilde{\boldsymbol{H}}_2+\tilde{\boldsymbol{E}}_2\times\tilde{\boldsymbol{H}}_2^*)dxdy}\\
&+jA\frac{\omega\varepsilon_0\int_{-\infty}^{\infty}\int_{-\infty}^{\infty}(N^2-N_1^2)\tilde{\boldsymbol{E}}_2^*\cdot\tilde{\boldsymbol{E}}_1\,dxdy}{\int_{-\infty}^{\infty}\int_{-\infty}^{\infty}\boldsymbol{u}_z\cdot(\tilde{\boldsymbol{E}}_2^*\times\tilde{\boldsymbol{H}}_2+\tilde{\boldsymbol{E}}_2\times\tilde{\boldsymbol{H}}_2^*)dxdy}\\
&+jB\frac{\omega\varepsilon_0\int_{-\infty}^{\infty}\int_{-\infty}^{\infty}(N^2-N_2^2)\tilde{\boldsymbol{E}}_2^*\cdot\tilde{\boldsymbol{E}}_2\,dxdy}{\int_{-\infty}^{\infty}\int_{-\infty}^{\infty}\boldsymbol{u}_z\cdot(\tilde{\boldsymbol{E}}_2^*\times\tilde{\boldsymbol{H}}_2+\tilde{\boldsymbol{E}}_2\times\tilde{\boldsymbol{H}}_2^*)dxdy}=0.
\end{aligned} \tag{2.9}$$

Here we separate the transverse and axial dependencies of the electromagnetic fields [17]:

$$\begin{cases} \tilde{\boldsymbol{E}}_p = \boldsymbol{E}_p \exp(-j\beta_p z) \\ \tilde{\boldsymbol{H}}_p = \boldsymbol{H}_p \exp(-j\beta_p z) \end{cases}, \qquad (p = 1,2) \tag{2.10}$$

where β_p (p = 1,2) is the propagation constant. Substituting Eq. (2.10) into Eqs. (2.8) and (2.9), we obtain [17]

$$\frac{dA}{dz} + c_{12}\frac{dB}{dz}\exp\left[-j(\beta_2 - \beta_1)z\right] + j\chi_1 A + j\kappa_{12} B \exp\left[-j(\beta_2 - \beta_1)z\right] = 0, \tag{2.11}$$

$$\frac{dB}{dz} + c_{21}\frac{dA}{dz}\exp\left[+j(\beta_2 - \beta_1)z\right] + j\chi_2 B + j\kappa_{21} A \exp\left[+j(\beta_2 - \beta_1)z\right] = 0, \tag{2.12}$$

where

$$\kappa_{pq} = \frac{\omega\varepsilon_0 \int_{-\infty}^{\infty}\int_{-\infty}^{\infty} (N^2 - N_q^2)\boldsymbol{E}_p^* \cdot \boldsymbol{E}_q dxdy}{\int_{-\infty}^{\infty}\int_{-\infty}^{\infty} \boldsymbol{u}_z \cdot (\boldsymbol{E}_p^* \times \boldsymbol{H}_p + \boldsymbol{E}_p \times \boldsymbol{H}_p^*) dxdy}, \tag{2.13}$$

$$c_{pq} = \frac{\int_{-\infty}^{\infty}\int_{-\infty}^{\infty} \boldsymbol{u}_z \cdot (\boldsymbol{E}_p^* \times \boldsymbol{H}_q + \boldsymbol{E}_q \times \boldsymbol{H}_p^*) dxdy}{\int_{-\infty}^{\infty}\int_{-\infty}^{\infty} \boldsymbol{u}_z \cdot (\boldsymbol{E}_p^* \times \boldsymbol{H}_p + \boldsymbol{E}_p \times \boldsymbol{H}_p^*) dxdy}, \tag{2.14}$$

$$\chi_p = \frac{\omega\varepsilon_0 \int_{-\infty}^{\infty}\int_{-\infty}^{\infty} (N^2 - N_p^2)\boldsymbol{E}_p^* \cdot \boldsymbol{E}_q dxdy}{\int_{-\infty}^{\infty}\int_{-\infty}^{\infty} \boldsymbol{u}_z \cdot (\boldsymbol{E}_p^* \times \boldsymbol{H}_p + \boldsymbol{E}_p \times \boldsymbol{H}_p^*) dxdy}, \tag{2.15}$$

and $\boldsymbol{u}_z$ means the outward-directed unit vector. The pair of p and q are either (p,q) = (1, 2) or (2, 1), respectively. κ_{pq} is a mode-coupling coefficient (MCC) of the directional coupler. c_{pq} represents the butt coupling coefficient between the two waveguides [19, 20]. χ_p can be neglected when two waveguides are sufficiently separated, since χ_p is much smaller than κ_{pq}. In most of the conventional analyses of the directional couplers, c_{pq} and χ_p were neglected and they are assumed to be $c_{pq} = \chi_p = 0$. However, both c_{pq} and χ_p should be taken into account in order to analyze the mode coupling effect strictly.

The optical power carried by the eigen mode in the waveguide p (p =1, 2) is expressed as

$$P_p = \frac{1}{2}\int_{-\infty}^{\infty}\int_{-\infty}^{\infty}\left(\boldsymbol{E}_p \times \boldsymbol{H}_p^*\right)\cdot \boldsymbol{u}_z dxdy. \quad \left(p = 1, 2\right) \tag{2.16}$$

It is know from this equation that the denominators of Eqs. (2.13) − (2.15) are equal to $4P_p$. Therefore, we can rewrite the Eq. (2.13) to be

$$\kappa_{pq} = \frac{\omega\varepsilon_0 \int_{-\infty}^{\infty}\int_{-\infty}^{\infty}(N^2 - N_q^2)\boldsymbol{E}_p^* \cdot \boldsymbol{E}_q dxdy}{4P_p}. \tag{2.17}$$

Fig. 2.2 shows the refractive index profile of two trench-assisted non-identical cores and the part outside the cores. The refractive-index distribution in the entire coupled region can be written as [21]

$$N^2(r,\theta) = N_1^2(r,\theta) + N_2^2(r,\theta) - n^2(r,\theta), \tag{2.18}$$

where $N_1(r, \theta)$ and $N_2(r, \theta)$ represent the refractive-index distribution of each core with trench structure, and $n(r, \theta)$ means the refractive-index distribution outside the cores, which are shown in Fig. 2.2(a), Fig. 2.2(b), and Fig. 2.2(c) respectively [21]. As shown in Fig. 2.3(a), $N^2-N_2^2$ is zero except the region inside core 1, so the difference of the refractive-index distribution inside the core 1 is $n_1^2-n_{\mathrm{cl}}^2$, while according to Fig. 2.3(b), $N^2-N_1^2$ is zero except the region inside core 2, so the difference of the refractive-index distribution inside the core 2 is $n_2^2-n_{\mathrm{cl}}^2$ [21]. Furthermore, the denominator of κ_{pq} equals $4P$, where P means the total power flow [17]. So the expression of κ_{pq} can be rewritten as

$$\kappa_{pq} = \frac{\omega\varepsilon_0}{4P_p}\int_0^{2\pi}\int_0^{a_{1-p}}\left(n_p^{\ 2} - n_{\mathrm{cl}}^{\ 2}\right)\boldsymbol{E}_p^* \cdot \boldsymbol{E}_q r dr d\theta, \tag{2.19}$$

where $\boldsymbol{E_p}$ and $\boldsymbol{E_q}$ represent the amplitude of electric field distribution of core p inside the range of core p, and the amplitude of electric field distribution of core q inside the range of core p, respectively. $a_{1\text{-}p}$ denotes the radius of core p.

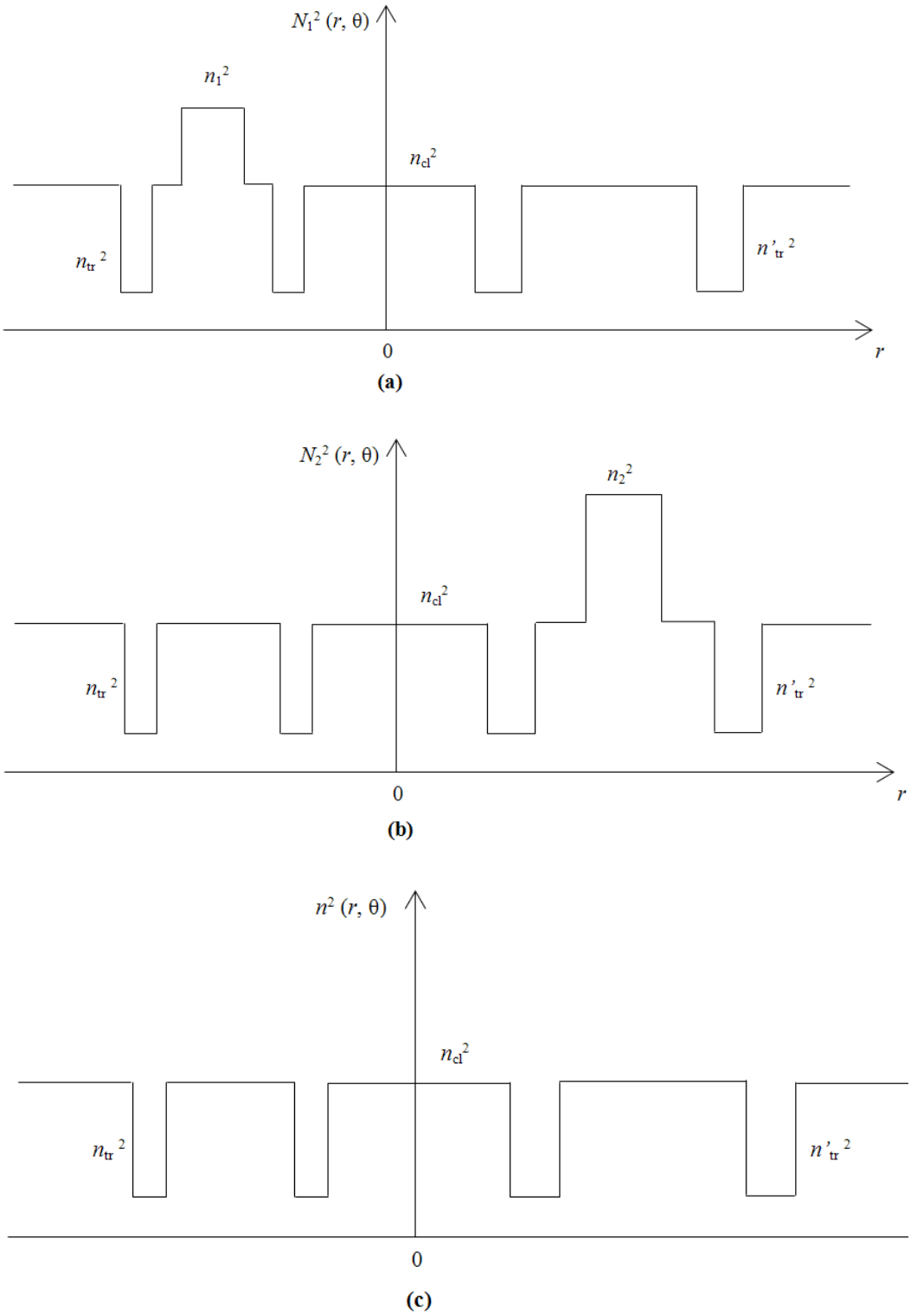

Fig. 2.2 The profile of refractive index in two trench-assisted non-identical cores and the part outside the cores.

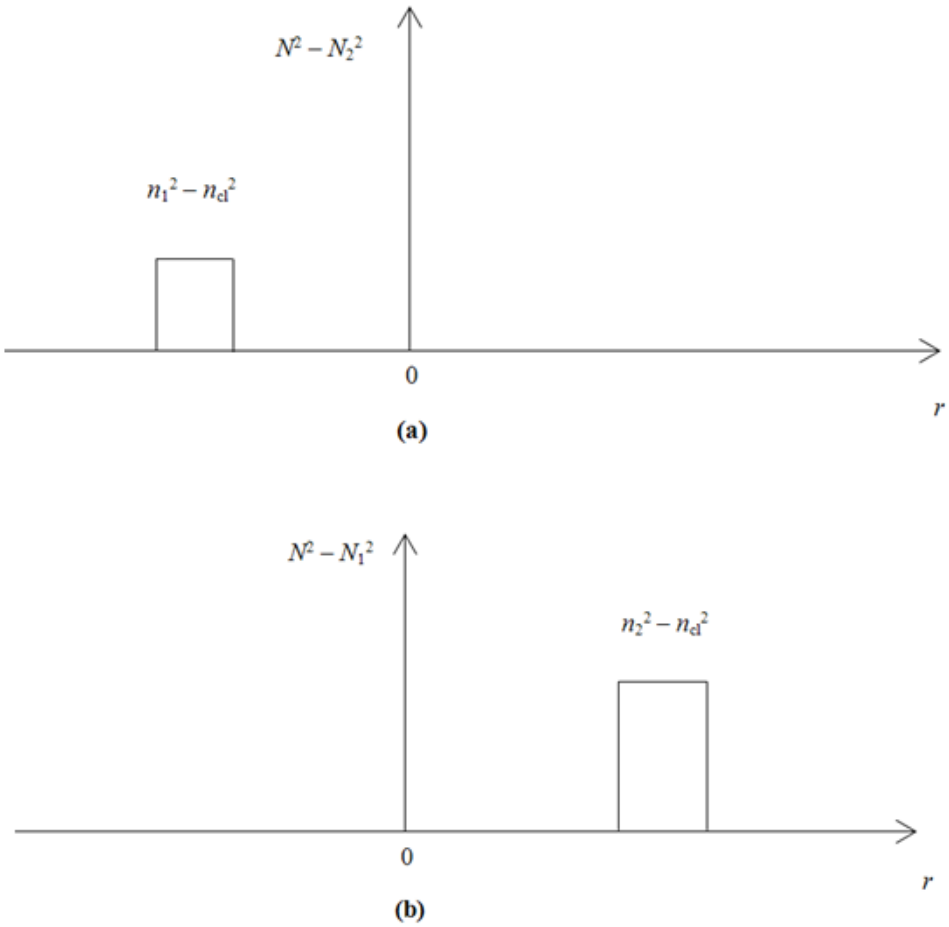

Fig. 2.3 Difference of the refractive-index distributions. (a) $N^2 - N_2^2$. (b) $N^2 - N_1^2$.

2.3 Calculation of mode-coupling coefficient between two trench-assisted cores based on analytical method

The electric fields in optical fibers are expressed in cylindrical coordinates as

$$\tilde{\boldsymbol{E}} = \boldsymbol{E}(r,\theta)e^{j(\omega t - \beta z)} \tag{2.20}$$

Substituting Eq. (2.20) into Maxwell's equation, we can obtain the wave equation as

$$\frac{\partial^2 E_z}{\partial r^2} + \frac{1}{r}\frac{\partial E_z}{\partial r} + \frac{1}{r^2}\frac{\partial^2 E_z}{\partial \theta^2} + \left[k^2 n(r,\theta)^2 - \beta^2\right]E_z = 0. \tag{2.21}$$

Here we define the wave number in the core m (m =1, 2), cladding and trench along the transversal direction as follows [21]:

$$\xi_m = \sqrt{n_m^2 k^2 - \beta_m^2}, \tag{2.22}$$

$$\sigma_m = \sqrt{\beta_m^2 - n_{cl}^2 k^2}, \tag{2.23}$$

$$\gamma_m = \sqrt{\beta_m^2 - n_{tr}^2 k^2}, \tag{2.24}$$

where β is the propagation constant and k is the wavenumber in a vacuum. The normalized frequency ($V_{1\text{-}m}$, $V_{2\text{-}m}$), the normalized transverse wave number in core m ($U_{1\text{-}m}$), that in cladding ($W_{1\text{-}m}$) and that in trench ($W_{2\text{-}m}$) can be expressed as follows [21]:

$$V_{1-m} = a_{1-m} k \sqrt{n_m^2 - n_{cl}^2}, \tag{2.25}$$

$$V_{2-m} = a_{1-m} k \sqrt{n_{cl}^2 - n_{tr}^2}, \tag{2.26}$$

$$W_{1-m} = a_{1-m}\sigma_m = 1.1428 V_{1-m} - 0.996, \tag{2.27}$$

$$U_{1-m} = a_{1-m}\xi_m = \sqrt{V_{1-m}^2 - W_{1-m}^2}, \tag{2.28}$$

$$W_{2-m} = a_{1-m}\gamma_m = \sqrt{V_{2-m}^2 + W_{1-m}{}^2}, \tag{2.29}$$

where $a_{1\text{-}m}$ is the radius of core m and Eq. (2.27) is the approximation which is in error by less than 0.2 percent for $1.5 \le V_{1\text{-}m} \le 2.5$ [22].

In the core region of fiber, the solutions for Eq. (2.21) of TM modes are the 0th-order Bessel function $J_0(\xi_m r_m)$ and the 0th-order Neumann function $N_0(\xi_m r_m)$ [17], respectively. However, $N_0(\xi_m r_m)$ diverges infinitely at r = 0. Therefore $J_0(\xi_m r_m)$ is the proper solution for the field in the core. In the cladding region of fiber, the solutions for Eq. (2.21) of TM modes are the modified Bessel function of the first kind $I_0(\sigma_m r_m)$ and modified Bessel functions of the second kind $K_0(\sigma_m r_m)$, respectively. For simplifying the calculation, we neglect the influence of $I_0(\sigma_m r_m)$ to the result and do approximation. Nevertheless, in hybrid modes, the solutions for Eq. (2.21) are given by the product of the nth-order Bessel functions and $\cos(n\theta+\psi)$. Thus, the z-components of the electric field can be obtained as

$$E_{mz} = \begin{cases} A_m J_n(\xi_m r_m)\cos(n\theta+\psi) & \text{(in Co } m\text{)} \\ B_m K_n(\sigma_m r_m)\cos(n\theta+\psi) & \text{(in IC } m\text{)} \\ C_m K_n(\gamma_m r_m)\cos(n\theta+\psi) & \text{(in Tr } m\text{)} \\ D_m K_n(\sigma_m r_m)\cos(n\theta+\psi) & \text{(in OC)} \\ E_m K_n(\gamma_m r_m)\cos(n\theta+\psi) & \text{(in Tr } m'\text{)} \\ F_m K_n(\sigma_m r_m)\cos(n\theta+\psi) & \text{(in IC } m'\text{)} \end{cases}, \tag{2.30}$$

the azimuthal dependency of the electric fields in axially symmetric fibers is expressed by $\cos(n\theta+\psi)$, where n is an integer and ψ denotes the phase. As shown in Fig. 2.4, core m, inner cladding between core m and trench m, trench m, outer cladding outside trench m, trench m' and inner cladding inside trench m' are abbreviated as Co m, IC m, Tr m, OC, Tr m', and IC m'. D is the core pitch, $a_{1\text{-}m}$ is the radius of core m, $a_{2\text{-}m}$ is the distance from the center of core m to the inner circumference of trench m, and $a_{3\text{-}m}$ is the distance from the center of core m to the outer circumference of trench m. R, R_1 and R_2 denote the distance between the center of core m to the objective point in IC m', the distance from the center of core m to the outer circumference of trench m' and the distance from the center of core m to the inner circumference of trench m', respectively [21].

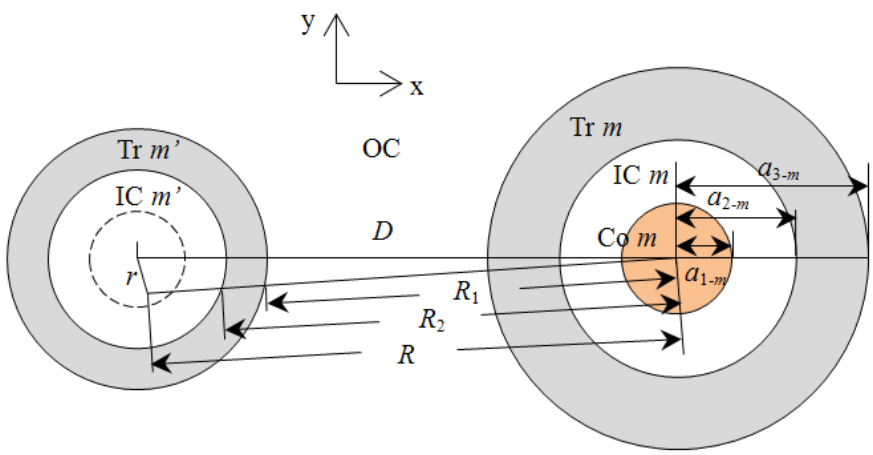

Fig. 2.4 The profile of core m with trench structures.

Without no doubt, the electric field should be continuous in each boundary, therefore the solutions in these six parts have the relationship which is shown as follows:

$$\begin{cases} A_m J_n(U_{1-m}) = B_m K_n(W_{1-m}) \\ B_m K_n(W_{1-m}\dfrac{a_{2-m}}{a_{1-m}}) = C_m K_n(W_{2-m}\dfrac{a_{2-m}}{a_{1-m}}) \\ C_m K_n(W_{2-m}\dfrac{a_{3-m}}{a_{1-m}}) = D_m K_n(W_{3-m}\dfrac{a_{3-m}}{a_{1-m}}). \\ D_m K_n(W_{3-m}\dfrac{R_1}{a_{1-m}}) = E_m K_n(W_{4-m}\dfrac{R_1}{a_{1-m}}) \\ E_m K_n(W_{4-m}\dfrac{R_2}{a_{1-m}}) = F_m K_n(W_{5-m}\dfrac{R_2}{a_{1-m}}) \end{cases} \tag{2.31}$$

Based on the boundary condition related above, the expression of D_m and F_m can be obtained, which are shown as follows:

$$D_m = L_m A_m, \tag{2.32}$$

$$F_m = Q_m A_m, \tag{2.33}$$

where

$$L_m = \frac{J_n(U_{1-m})K_n(W_{1-m}\dfrac{a_{2-m}}{a_{1-m}})K_n(W_{2-m}\dfrac{a_{3-m}}{a_{1-m}})}{K_n(W_{1-m})K_n(W_{2-m}\dfrac{a_{2-m}}{a_{1-m}})K_n(W_{3-m}\dfrac{a_{3-m}}{a_{1-m}})}, \tag{2.34}$$

$$Q_m = L_m \frac{K_n(W_{3-m}\dfrac{R_1}{a_{1-m}})K_n(W_{4-m}\dfrac{R_2}{a_{1-m}})}{K_n(W_{4-m}\dfrac{R_1}{a_{1-m}})K_n(W_{5-m}\dfrac{R_2}{a_{1-m}})}. \tag{2.35}$$

And based on [17], the amplitude coefficient A_m of the field is given by

$$A_m = \frac{U_{1-m}W_{1-m}}{\beta_m a_{1-m}{}^2 V_{1-m} J_1(U_{1-m})}\sqrt{\frac{2P}{\pi\varepsilon_0 n_{1-m} c}}, \tag{2.36}$$

where c is the velocity of light in a vacuum. Fig. 2.5 illustrates the geometries for the calculation of the coupling coefficient [21]. Setting n = 1 and using the equation of electric fields in [17] by assuming $s = s_1 = s_2 = -1$, the electronic fields of the fundamental HE_{11} mode inside the core p can be express as follows [21]:

$$E_p = \begin{cases} E_{px} = -jA_p\beta_p \dfrac{a_{1-p}}{U_{1-p}} J_0(U_{1-p}\dfrac{r}{a_{1-p}})\cos\psi \\ E_{py} = jA_p\beta_p \dfrac{a_{1-p}}{U_{1-p}} J_0(U_{1-p}\dfrac{r}{a_{1-p}})\sin\psi \\ E_{pz} = A_p J_1(U_{1-p}\dfrac{r}{a_{1-p}})\cos(\theta+\psi) \end{cases}, \tag{2.37}$$

$$E_q = \begin{cases} E_{qx} = -jQ_q A_q\beta_q \dfrac{a_{1-q}}{W_{1-q}} K_0(W_{1-q}\dfrac{R}{a_{1-q}})\cos\psi \\ E_{qy} = jQ_q A_q\beta_q \dfrac{a_{1-q}}{W_{1-q}} K_0(W_{1-q}\dfrac{R}{a_{1-q}})\sin\psi \\ E_{qz} = Q_q A_q K_1(W_{1-q}\dfrac{R}{a_{1-q}})\cos(\Theta+\psi) \end{cases}. \tag{2.38}$$

where

$$R = \sqrt{D^2 + r^2 - 2Dr\cos\theta} \approx D - r\cos\theta, \tag{2.39}$$

$$a_{3-p} = \sqrt{D^2 + R_1^2 - 2DR_1\cos(\pi-\Theta)} \approx D - R_1\cos(\pi-\Theta), \tag{2.40}$$

$$r = \sqrt{D^2 + R^2 - 2DR\cos(\pi-\Theta)} \approx D - R\cos(\pi-\Theta), \tag{2.41}$$

$$\Rightarrow R_1 \approx \frac{(D-a_{3-p})(D-r\cos\theta)}{D-r}. \tag{2.42}$$

In the same principle,

$$R_2 \approx \frac{(D-a_{2-p})(D-r\cos\theta)}{D-r}. \tag{2.43}$$

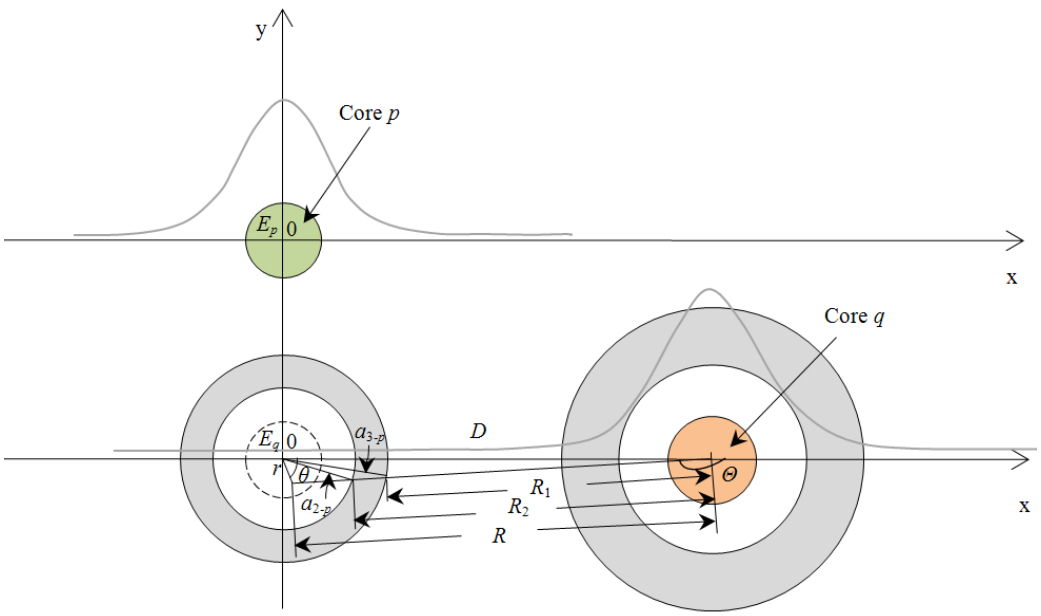

Fig. 2.5 Geometries for the calculation of the coupling coefficient.

Inside Eq. (2.19), $\boldsymbol{E_p}^* \cdot \boldsymbol{E_q}$ can be expressed as [21]

$$\begin{aligned}\boldsymbol{E_p}^* \cdot \boldsymbol{E_q} &= Q_q A_p A_q \beta_p \beta_q \frac{a_{1-p} a_{1-q}}{U_{1-p} W_{1-q}} J_0(U_{1-p} \frac{r}{a_{1-p}}) K_0(W_{1-q} \frac{R}{a_{1-q}}) \\ &+ Q_q A_p A_q J_1(U_{1-p} \frac{r}{a_{1-p}}) K_1(W_{1-q} \frac{R}{a_{1-q}}) \cos(\theta + \psi) \cos(\Theta + \psi) .\end{aligned} \tag{2.44}$$

Since the second term of the right-hand side of the equation above is sufficiently smaller than the first term, the integration of the first part in the square brackets of Eq. (2.19) becomes:

$$\begin{aligned}S_1 &= \int_0^{2\pi} \int_0^{a_{1-p}} (n_p^{\ 2} - n_{\mathrm{cl}}^{\ 2}) \boldsymbol{E_p}^* \cdot \boldsymbol{E_q} r dr d\theta = (n_p^{\ 2} - n_{\mathrm{cl}}^{\ 2}) L_q A_p A_q \beta_p \beta_q \frac{a_{1-p} a_{1-q}}{U_{1-p} W_{1-q}} \\ &\times \int_0^{2\pi} \int_0^{a_{1-p}} J_0(U_{1-p} \frac{r}{a_{1-p}}) K_0(W_{1-q} \frac{R}{a_{1-q}}) \frac{K_1(P_1 \frac{D - r\cos\theta}{D - r}) K_1(Y_1 \frac{D - r\cos\theta}{D - r})}{K_1(P_2 \frac{D - r\cos\theta}{D - r}) K_1(Y_2 \frac{D - r\cos\theta}{D - r})} r dr d\theta ,\end{aligned} \tag{2.45}$$

where $P_1=W_{1-q}(D-a_{3-p})/a_{1-q}$, $P_2=W_{2-q}(D-a_{3-p})/a_{1-q}$, $Y_1=W_{2-q}(D-a_{2-p})/a_{1-q}$, $Y_1=W_{1-q}(D-a_{2-p})/a_{1-q}$.When the argument of the modified Bessel function $K_n(z)$ in Eq. (2.45) is large, it can be approximated as

$$K_n(z) \cong \sqrt{\frac{\pi}{2z}} \exp(-z). \tag{2.46}$$

Substitution of Eq. (2.46) into Eq. (2.45) gives [21]

$$\begin{aligned} S_1 &= (n_p{}^2 - n_{\mathrm{cl}}{}^2) L_q A_p A_q \beta_p \beta_q \frac{a_{1-p}\ a_{1-q}}{U_{1-p}\ W_{1-q}} \sqrt{\frac{\pi a_{1-q}}{2W_{1-q}D}} \exp(-W_{1-q}\frac{D}{a_{1-q}}) \\ &\times \int_0^{a_{1-p}} J_0(U_{1-p}\frac{r}{a_{1-p}}) \exp[(P_2 - P_1 + Y_2 - Y_1)\frac{D}{D-r}] r dr \int_0^{2\pi} \exp[(\frac{W_{1-q}}{a_{1-q}} - \frac{P_2 - P_1 + Y_2 - Y_1}{D-r}) r\cos\theta] d\theta . \end{aligned} \tag{2.47}$$

By using the integral formulas of the Bessel functions [23]:

$$I_0(z) = \frac{1}{\pi}\int_0^{\pi} \exp(z\cos\theta) d\theta, \tag{2.48}$$

the coupling coefficient κ_{pq} can be expressed as [21]

$$\begin{aligned} \kappa_{pq} &= \frac{k(n_p{}^2 - n_{\mathrm{cl}}{}^2) W_{1-p} U_{1-q} L_q \sqrt{\frac{\pi a_{1-q}}{2W_{1-q}D}} \exp(-W_{1-q}\frac{D}{a_{1-q}})}{\sqrt{n_p n_q} a_{1-p} a_{1-q} V_{1-p} V_{1-q} J_1(U_{1-p}) J_1(U_{1-q})} \\ &\times \int_0^{a_{1-p}} J_0(U_{1-p}\frac{r}{a_{1-p}}) I_0[(\frac{W_{1-q}}{a_{1-q}} - \frac{P_2 - P_1 + Y_2 - Y_1}{D-r}) r] \exp[(P_2 - P_1 + Y_2 - Y_1)\frac{D}{D-r}] r dr . \end{aligned} \tag{2.49}$$

where

$$P_2 - P_1 + Y_2 - Y_1 = (W_{1-q} - W_{2-q})\frac{a_{3-q} - a_{2-q}}{a_{1-q}}, \tag{2.50}$$

$$L_q = \frac{J_1(U_{1-q})K_1(W_{1-q}\frac{a_{2-q}}{a_{1-q}})K_1(W_{2-q}\frac{a_{3-q}}{a_{1-q}})}{K_1(W_{1-q})K_1(W_{2-m}\frac{a_{2-q}}{a_{1-q}})K_1(W_{3-q}\frac{a_{3-q}}{a_{1-q}})}$$

$$= \frac{J_1(U_{1-q})}{K_1(W_{1-q})}\frac{\sqrt{W_{2-q}\frac{a_{2-q}}{a_{1-q}}W_{1-q}\frac{a_{3-q}}{a_{1-q}}}}{\sqrt{W_{1-q}\frac{a_{2-q}}{a_{1-q}}W_{2-q}\frac{a_{3-q}}{a_{1-q}}}}\exp(W_{2-q}\frac{a_{2-q}}{a_{1-q}} + W_{1-q}\frac{a_{3-q}}{a_{1-q}} - W_{1-q}\frac{a_{2-q}}{a_{1-q}} - W_{2-q}\frac{a_{3-q}}{a_{1-q}}) \tag{2.51}$$

$$= \frac{J_1(U_{1-q})}{K_1(W_{1-q})}\exp[(W_{1-q} - W_{2-q})\frac{a_{3-q} - a_{2-q}}{a_{1-q}}].$$

And in the integration, r is much smaller than the core-to-core distance D, so the components $\frac{r}{D-r} \approx 0$, and $\frac{D}{D-r} \approx 1$. Therefore, Eq. (2.49) can be simplified to be [21]

$$\kappa_{pq} = \frac{k(n_p^{\ 2} - n_{\mathrm{cl}}^{\ 2})W_{1-p}U_{1-q}\sqrt{\frac{\pi a_{1-q}}{2W_{1-q}D}}\exp[-W_{1-q}\frac{D}{a_{1-q}} + 2(W_{1-q} - W_{2-q})\frac{a_{3-q} - a_{2-q}}{a_{1-q}}]}{\sqrt{n_p n_q}a_{1-p}a_{1-q}V_{1-p}V_{1-q}J_1(U_{1-p})J_1(U_{1-q})} \times \int_0^{a_{1-p}} J_0(U_{1-p}\frac{r}{a_{1-p}})I_0(\frac{W_{1-q}}{a_{1-q}}r)rdr\,. \tag{2.52}$$

For two identical trench-assisted cores, κ_{pq} can be expressed as [24]

$$\kappa_{12} = \kappa_{21} = \frac{\sqrt{\Delta_1}}{a_1}\frac{U_1^2}{V_1^3K_1^2(W_1)}\sqrt{\frac{\pi a_1}{W_1 D}}\exp[-\frac{W_1 D + 2(W_2 - W_1)w_{tr}}{a_1}], \tag{2.53}$$

where w_{tr} means the thickness of the trench layer.

2.4 Comparison with the mode-coupling coefficient based on finite element method

To solve Eq. (2.19), we can use either analytical approach or finite element method (FEM). In the above section, we chose the analytical approach and did an approximation that we assumed the z-components of electric field outside the core converge quickly so that we neglected the effect of the first kind modified Bessel function in the field outside the core. On the other hand, we can also take advantage of FEM to obtain the mode-coupling coefficient. In the finite element method (FEM), the domain of the problem is discretized into small elements. The solution of the problem is approximated in each element, and it is connected at the nodal points to from the solution model in the entire analysis domain. Therefore, FEM is applicable to complicated domain structures and to problems in which electromagnetic fields are localized. For the application of FEM, we adopted commercial finite element analysis software — COMSOL Multiphysics to simulate the electric field distribution of each model and then integrated the data in MATLAB to figure out the MCC between the neighboring cores.

In order to estimate the accuracy degree of the approximate analytical solution (AAS) discussed in last subsection, we compare it with FEM by calculating the coupling coefficient between adjacent cores in homogeneous trench assisted multi-core fiber (Homo-TA-MCF). Here we use the Homo-TA-7-core fiber as a model to do this comparison. Fig. 2.6 and Fig. 2.7 show index profile of a core with trench and the schematic of the Homo-TA-7-core model. The coiling diameter of the fiber was assumed to be 210 mm, which is the same with the value in [25]. The parameters which we used are summarized in Tab. 2.1. Fig. 2.8 illustrates the length dependence of simulated crosstalk (*XT*) of step-index MCF (S-MCF) and trench-assisted MCF (TA-MCF) at 1550-nm wavelength. The blue solid line relates the simulation result of S-MCF. On the other hand, the red solid line represents the result of TA-MCF which is calculated by using the above-mentioned method and the green solid line represents the result of TA-MCF that is obtained by using the FEM [16]. The error between crosstalk values which were calculated by these two methods is about −0.4 dB, a sufficiently small value, which proves the feasibility of this analytical method.

The numerical results in Fig. 2.8 have proved that the approximate analytical solution (AAS) is feasible when $r_2/r_1 = 2.0$. But we have to analyze the MCC at other locations of trench layer to further prove its feasibility, therefore, we compared the MCC between two identical cores based on AAS with the one based on FEM. For the comparison, we calculated the MCC between a couple of Homo-TA-cores with $r_1 = 4$ μm, $\Delta_1 = 0.375$ %, $\Delta_2 = -0.5$ % and core pitch (Λ) = 40 μm.

From the comparison results shown in Fig. 2.9, we find that when r_2/r_1 becomes larger than 2.0, the result of MCC based on AAS agrees well with the one based on FEM, which implies that if the first kind modified Bessel function outside the core (r_1 = 4 μm, Δ_1= 0.375 %) is neglected in this case, the MCC based on the AAS does not have a large error. Nevertheless, once r_2/r_1 becomes smaller than 2.0, in other words, when the trench structure gets very close to the core, the difference between the results based on these two approaches will increase immediately. Therefore, the AAS proposed in [21] cannot figure out accurate MCC in all the situations. Since we aim at high core density, Λ is required to be as small as possible, which asks us to deploy the trench layer close to the core. Thus, we use FEM hereafter instead of AAS to obtain more accurate MCC for the Hetero-TA-MCF and this conclusion is presented in [26].

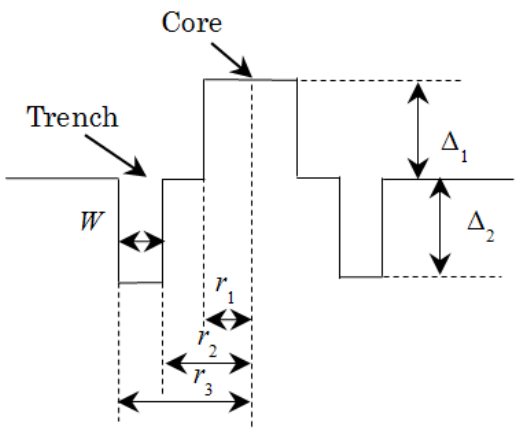

Fig. 2.6 Schematic of a core with index trench.

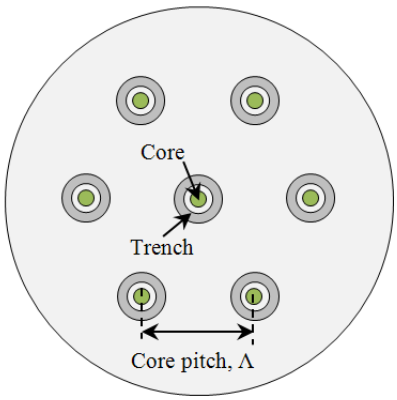

Fig. 2.7 Cross section of Homo-TA-7-core model.

Table 2.1 Structural parameters for calculation

Parameter	Unit	Trench	Step
r_1	[μm]	4.00	4.00
r_2/r_1	-	2.00	-
r_3/r_1	-	3.00	-
W/r_1	-	1.00	-
Δ_1	[%]	0.375	0.375
Δ_2	[%]	−0.65	-
n_{cl}	-	1.45	1.45
Λ	[μm]	40	40
R	[mm]	105	105

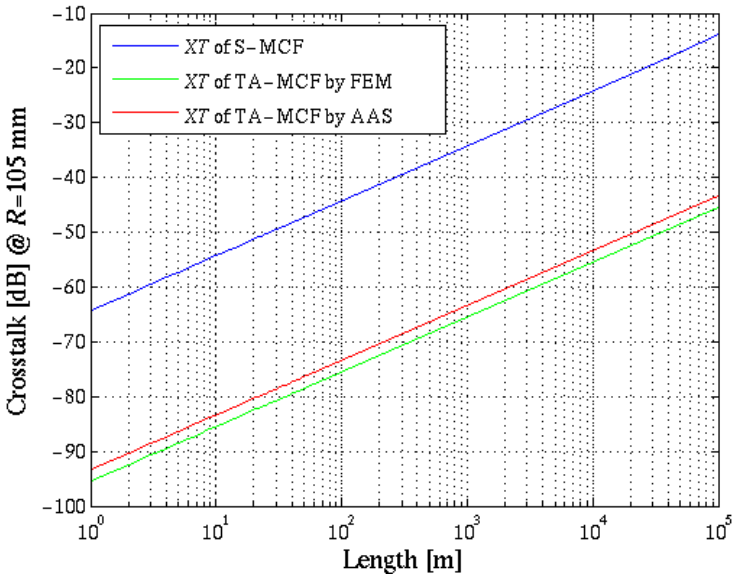

Fig. 2.8 Simulated crosstalk at 1550-nm wavelength as function of length.

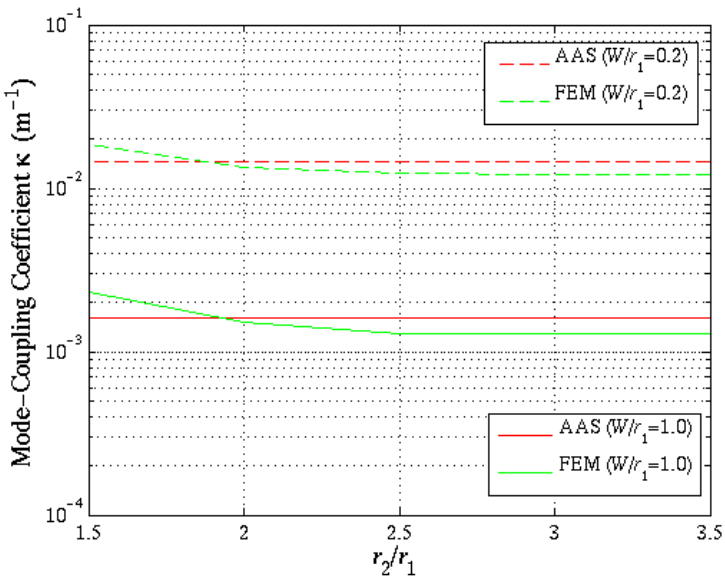

Fig. 2.9 Comparison of MCC between Homo-TA-cores based on AAS and FEM.

2.5 Derivation of mode-coupling coefficient based on mode interference

The mode-coupling effect in two identical directional couplers can be analyzed by the interference phenomena between the even and odd modes, as shown in Fig. 2.10 [27]. When we neglect the higher-order modes, the electric field in the directional coupler can be approximated by the summation of the even mode (first-order mode in the five-layer waveguide) and the odd mode (second-order mode in the five-layer waveguide):

$$E(x,z) = E_e(x)\exp(-j\beta_e z) + E_o(x)\exp(-j\beta_o z), \tag{2.54}$$

where $E_e(x)$ and β_e denote electric field and propagation constant of the even mode and $E_o(x)$ and β_o denote those of the odd mode, respectively.

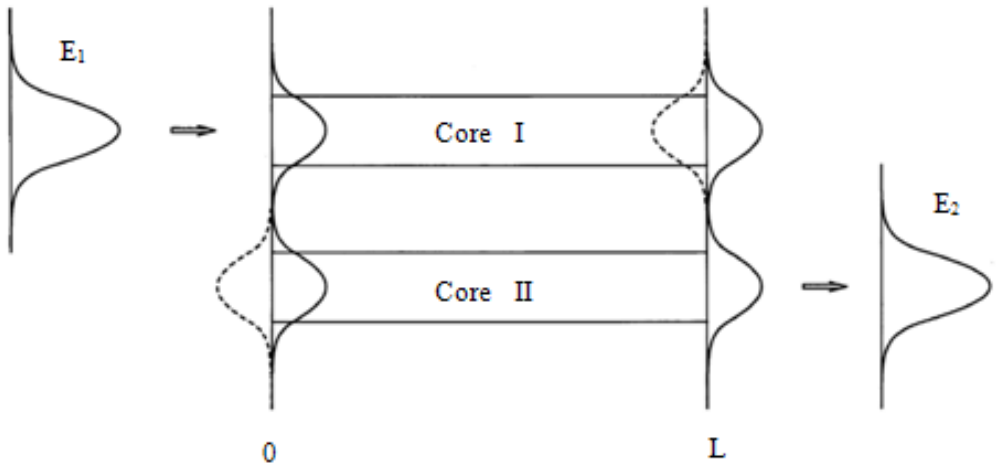

Fig. 2.10 Even (solid line) and odd (dotted line) modes in the five-layer slab waveguide.

The incident electric field, which is coupled to waveguide I at $z = 0$, is expressed by

$$|E(x,0)| = |E_e(x) + E_o(x)| = E_1(x). \tag{2.55}$$

Here $E_1(x)$ denotes the eigen mode of waveguide I. When the cores of waveguides I and II are not so close, this expression holds with good accuracy. The electric field amplitude at z is given, from (2.54), as

$$|E(x,z)| = |E_e(x) + E_o(x)\exp[j(\beta_e - \beta_o)z]|. \tag{2.56}$$

Electric field distribution at $z = \pi/(\beta_e - \beta_o)$ is then given by

$$|E(x,z)| = |E_e(x) + E_o(x)| = E_2(x), \tag{2.57}$$

where $E_2(x)$ denotes the eigen mode of waveguide II. Eq. (2.57) means that the incident field coupled to waveguide I shifted to waveguide II at the distance

$$L_c = \frac{\pi}{\beta_e - \beta_o}. \tag{2.58}$$

L_c is a coupling length and L_c can also be expressed as $L_c = \pi/(2\kappa)$. Hence, the mode-coupling coefficient can be written as

$$\kappa = \frac{\pi}{2L_c} = \frac{\beta_e - \beta_o}{2}. \tag{2.59}$$

2.6 Conclusion

In this chapter, we described the derivation of mode-coupling coefficient (MCC) based on perturbation theory and then gave the general calculation method by using approximate analytical solution (ASS). Moreover, we also used finite element method to prove the feasibility of the approximate analytical approach and we found that when r_2/r_1 becomes larger than 2.0, the result of MCC based on AAS agrees well with the one based on FEM, but once r_2/r_1 becomes smaller than 2.0, the difference between the results based on these two approaches will increase immediately. At last, we introduced another simple way to calculate MCC between two identical cores based on interference phenomena.

Chapter 3 Calculation method for inter-core crosstalk under bent condition of fiber

3.1 Introduction

In the practical use of fiber, we cannot guarantee that fiber transmit the optical signals in straight direction all the time. On the other words, bent fiber phenomenon cannot be avoided. Therefore, in order to evaluate a fiber, how to calculate the crosstalk under the bent condition is an important issue.

As we all known, the coupled-mode theory is very effective for investigation of the coupling between waveguides [28]. So in the section 3.2, we introduce the calculation method of crosstalk between two cores in the bent fiber based on coupled-mode theory. On the other hand, the coupled-power theory is also available that treats the power rather than the amplitude for coupling by introducing an ensemble averaging [27, 29]. In the section 3.3, we formulate the coupled-power theory for a two-core bent fiber.

3.2 Calculation of crosstalk in bent fiber based on coupled-mode theory

We select a two-core fiber with a constant bending radius and a constant twisting rate, and then analyze the stochastic inter-core crosstalk. The coupled-mode theory leads to the following coupling-mode equation (CME)

$$\frac{\partial A_n}{\partial z} = \sum_{m \neq n} -j\kappa_{nm} \exp\left\{-j\left[\phi_m(z) - \phi_n(z)\right]\right\} A_m, \tag{3.1}$$

where A is the slowly varying complex amplitude of the electric field, κ_{nm} is the mode-coupling coefficient from core m to core n, and z is the longitudinal axis of the fiber. So the dominant crosstalk changes can be approximate as following discrete changes [14]:

$$\begin{aligned} A_{n,N} &= A_{n,N-1} - jK_{nm} \exp\left[-j\phi_{rnd}(N)\right] A_{m,N-1} \\ &= A_{n,0} - jK_{nm} \sum_{l=1}^{N} \exp\left[-j\phi_{rnd}(l)\right] A_{m,l-1}, \end{aligned} \tag{3.2}$$

where $A_{n,N}$ represents the amplitude A of core n after the N-th phase-matching point, ϕ_{rnd} is the

random phase offset between core m and core n, and K_{nm} is the coefficient for the discrete changes caused by the coupling from core m to core n. Here, the crosstalk is assumed to be adequately low so that $A_{m,N}$ can be approximated by $A_{m,0} = 1$ and the crosstalk (XT) is $|A_{n,N}|^2$. In [14], the absolute value of K_{nm} between two identical cores can be derived as follows:

$$|K_{nm}| = |K_{mn}| = |K| \cong \sqrt{\frac{\kappa^2}{\beta}\frac{R}{D_{nm}}\frac{2\pi}{\gamma}}, \tag{3.3}$$

where γ represents the twist rate and D_{nm} is the core-to-core distance between core m and core n.

Variance σ^2 can be expressed as

$$\sigma^2 = E(x^2) - [E(x)]^2. \tag{3.4}$$

So the variance σ^2 of $\mathrm{Re}[K_{nm}\exp(j\phi_{rnd})]$ and $\mathrm{Im}[K_{nm}\exp(j\phi_{rnd})]$ can be expressed as $|K_{nm}|^2/2$, since $E[\cos(j\phi_{rnd})]$ and $E[\sin(j\phi_{rnd})]$ in one period or multiple periods is 0. Thus, $\mathrm{Re}(A_{n,N})$ and $\mathrm{Im}(A_{n,N})$ have Gaussian profiles whose variance σ^2 is $N|K_{nm}|^2/2$, if N is adequately large due to the statistical independence and the central limit theorem. Here, N can be assumed to be $L\gamma/\pi$ where L is the length of fiber. Therefore, the variance σ_2^2 of $\mathrm{Re}(A_{n,N})$ and $\mathrm{Im}(A_{n,N})$ can be written as

$$\sigma_2^2 = \frac{\kappa^2}{\beta}\frac{R}{D_{nm}}L. \tag{3.5}$$

Because $\mathrm{Re}(A_{n,N})$ and $\mathrm{Im}(A_{n,N})$ are two independent random variable, and $\mathrm{Re}(A_{n,N})/\sigma_2^2 \sim N(0, 1)$, $\mathrm{Im}(A_{n,N})/\sigma_2^2 \sim N(0, 1)$, so $|A_{n,N}|^2/\sigma_2^2$ which is equaling $[\mathrm{Re}(A_{n,N})/\sigma_2]^2+[\mathrm{Im}(A_{n,N})/\sigma_2]^2$ has a chi-square distribution with two degrees of freedom. Hence, the average value of XT/σ_2^2 is the freedom degree 2, and the mean crosstalk XT_μ can be obtained as

$$XT_\mu = 2\sigma_2^2 = 2\frac{\kappa^2}{\beta}\frac{R}{D_{nm}}L \tag{3.6}$$

3.3 Calculation of crosstalk in bent fiber based on coupled-power theory

In coupled-power theory, coupled-power equations (CPE) are written as [29]

$$\frac{dP_m}{dz} = \sum_{n \neq m} h_{mn}(z)[P_n(z) - P_m(z)], \tag{3.7}$$

where P_m is the average power in core m and h_{mn} is the power-coupling coefficient (PCC).

For loss-less MCFs, MCCs should be symmetric, $\kappa_{mn} = \kappa_{nm}$. However, for non-identical cores, they are not symmetric, therefore MCC can be redefined as [30]

$$K_{mn} = K_{nm} = \frac{\kappa_{mn} + \kappa_{nm}}{2}. \tag{3.8}$$

As PCCs should also be symmetric, the starting point for deriving PCCs in CMEs with redefined MCCs, K_{nm}=K_{mn}. After considering the phase change and random part caused by bend and twist, we can obtain PCC as follows: [30]

$$P_m(z) = zP_n(0)\frac{K_{mn}^2}{2}\int_{-\infty}^{\infty} \exp\left(j\Delta\beta'_{mn}\varsigma\right)R(\varsigma)d\varsigma, \tag{3.9}$$

where $R(\zeta)$ is an autocorrelation function for the random part and $\Delta\beta'_{mn}$ represents the local propagation-constant difference at $z = z'$ under the bent condition. Therefore, local PCC with the power spectral density can be expressed as

$$h_{mn} = \frac{P_m(z)}{zP_n(z)} = \frac{K_{mn}^2}{2}S(\Delta\beta'_{mn}), \tag{3.10}$$

where $S(\Delta\beta'_{mn})$ is the Fourier transform of the autocorrelation function.

There are three types of autocorrelation functions, which are based on exponential autocorrelation function (EAF), Gaussian autocorrelation function (GAF), and triangular autocorrelation function (TAF), respectively. $R(\zeta)$ of EAF is $\exp(-|\zeta|/d_c)$, $R(\zeta)$ of GAF is $\exp[(-(|\zeta|/d_c)^2]$, and $R(\zeta)$ of TAF is $1-(|\zeta|/d_c)$ when $|\zeta| \leq d_c$ and 0 when $|\zeta| > d_c$, where d_c is the correlation length. The corresponding PCCs are, for EAF,

$$h_{mn}(z) = \frac{2K^2{}_{mn} d_c}{1 + \left[\Delta\beta'_{mn}(z) d_c\right]^2}, \tag{3.11}$$

For GAF,

$$h_{mn}(z) = \frac{\sqrt{\pi} K_{mn}^2 d_c}{2} \exp\left(-\left[\frac{\Delta\beta'_{mn}(z) d_c}{2}\right]^2\right), \tag{3.12}$$

and for TAF,

$$h_{mn}(z) = \frac{K_{mn}^2 d_c \sin^2\left[\Delta\beta'_{mn}(z) d_c / 2\right]}{2\left[\Delta\beta'_{mn}(z) d_c / 2\right]^2}. \tag{3.13}$$

Using the average PCC, the crosstalk (*XT*) between two cores with length *L* is estimated as

$$XT = \tanh\left(\bar{h}_{mn} L\right). \tag{3.14}$$

If the crosstalk is very small, it can be approximated as

$$XT \cong \bar{h}_{mn} L. \tag{3.15}$$

3.4 Conclusion

In this chapter, we introduced the calculation method for power-coupling coefficient (PCC) and crosstalk under the bent condition based on coupled-mode theory and coupled-power theory. The crosstalk expression based on the coupled-mode theory which is proposed by [14] can obtain the crosstalk between two identical cores quickly. On the other hand, after redefining the mode-coupling coefficient, the coupled-power theory can be used to solve the PCC not only between the identical but also non-identical cores. It is also proved that the simulation results of coupled-power theory agree well with the measurement results in [31] when we choose appropriate correlation length.

Chapter 4 Design and analysis of one-ring layout heterogeneous trench-assisted multi-core fiber (Hetero-TA-MCF) with ultra-low crosstalk and high core density

4.1 Introduction

How to cope with the exponentially increasing demand for transmission capacity per fiber is a hot topic nowadays. As an approach to achieve space division multiplexing (SDM), multi-core fiber (MCF) has been proposed to solve the issue related above [1].

Recently, several kinds of homogeneous MCFs (Homo-MCFs) in which all the cores are identical to each other have been designed and fabricated in order to realize long-haul transmission with low crosstalk [3, 32]. Furthermore, a type of optical fiber called heterogeneous MCF (Hetero-MCF) has been proposed to obtain much lower crosstalk, in which there are not only identical cores but also non-identical cores and the cores are more closely packed in a definite space [4]. On the other hand, a trench-assisted MCF (TA-MCF) that realizes much smaller crosstalk and larger effective area (A_{eff}) comparing to MCF with step-index profile also has been proposed [25]. It has been proved that the crosstalk between the identical cores will become larger and larger as bending radius (R) increases [32]. However the Hetero-MCF is insensitive to the bending radius after the R reaching a threshold value which was called R_{pk} in [14]. Moreover, if the cores have slight differences in their core radii and core refractive indices, the maximum power transferred between the cores goes down drastically [4]. Therefore, Hetero-MCF is a good candidate for the research of fiber under the bending condition. In addition, if we want to accommodate more cores inside the fiber, the core pitch between each pair of cores needs to be reduced. But small core pitch will result in a large crosstalk between cores. So in order to lower the crosstalk and meanwhile increase the core number in the fiber, a Hetero-MCF which has an index trench structure around each core (Hetero-TA-MCF) can be a solution.

In this chapter, at first, we discuss how to select Hetero-TA-cores with same effective area (A_{eff}). Secondly, we analyze how to design the trench location, trench thickness, and the relative refractive-index difference between trench and cladding (Δ_2) to optimize the crosstalk, R_{pk} and relative core multiplicity factor (*RCMF*). At last, we give the optimum scheme for

Hetero-TA-MCF with ultra-low crosstalk and high density of cores to realize a large-scale SDM transmission.

4.2 Design method of Hetero-TA-MCF

We design a kind of Hetero-TA-MCF with a ring layout for this work. If several layers of cores are set inside the fiber, the cut-off wavelengths of the interior cores tend to be longer than that of the exterior cores [25]. This is due to the tight confinements in the interior cores which are caused by the trench structure deployed around each core. Moreover, excessive crosstalk degradation will also happen in the inner cores [33]. Thus, we only arrange one layer of cores with a ring layout for the Hetero-TA-MCF. The design concept model is shown as Fig. 4.1 and Fig. 4.2 illustrates the schematic of a core with index trench. In the Fig. 4.2, r_1, r_2, r_3, W, Δ_1, and Δ_2 stand for core radius, the distance between the center of core and the inner circumference of trench, the distance between the center of core and outer circumference of trench, the thickness of the trench layer, the relative refractive-index difference between core and cladding, and the relative refractive-index difference between trench and cladding, respectively. Here, we only choose two sorts of non-identical cores inside the Hetero-TA-MCF and the reason will be explained in the next section. In addition, because we do not know the appropriate core number at the beginning, we use the small black dots shown in the Fig. 4.1 to represent the expansion of cores.

To design a Hetero-TA-MCF, we should firstly determine the location and thickness of the trench structure, secondly under the target value of A_{eff}, select cores parameters (such as core radii and refractive indices), thirdly set the core pitch, and at last according to the required outer cladding thickness and the limit value of cladding diameter, determine the core number. When we design a Hetero-TA-MCF, several factors that influence the properties of fiber should be taken into account. They are macro-bending loss [34], micro-bending loss [35], core effective are (A_{eff}), crosstalk, R_{pk} and *RCMF*. Based on the core-selecting process analyzed in [21], we can know that R_{pk} has a trade-off relationship with the available maximum A_{eff}, the required cores and cladding diameter are designed under the limit of macro-bending loss and micro-bending loss. Therefore, we only focus on the analysis of crosstalk, R_{pk}, and *RCMF*, which are the optimized objects in this chapter and also play important roles in evaluating a superior Hetero-TA-MCF. However, optimizing a Hetero-TA-MCF does not mean that every property of MCF can reach an optimized value. We should make compromises among crosstalk, A_{eff}, R_{pk} and *RCMF* through the design process and then propose a relative optimized design scheme for the Hetero-TA-MCF.

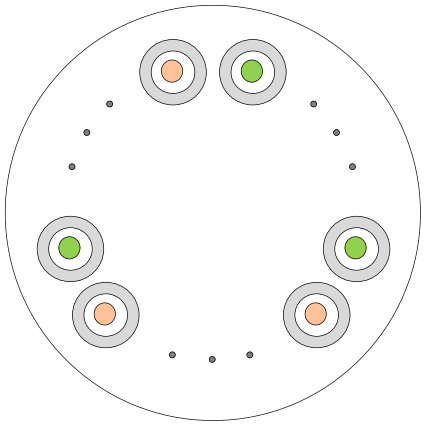

Fig. 4.1 Design concept model of Hetero-TA-MCF.

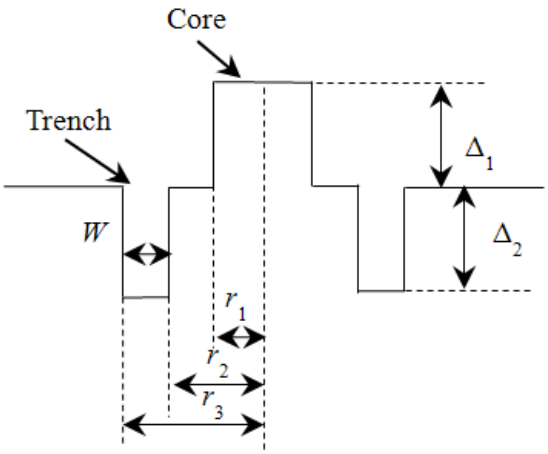

Fig. 4.2 Schematic of a core with index trench.

A. Selection of Hetero-TA-cores

Fig. 4.3 illustrates the core effective index (n_{eff}) and effective area (A_{eff}) of the fundamental mode at 1550-nm wavelength as function of core r_1 and the core Δ_1, where (a) r_2/r_1 = 2.0, W/r_1 = 1.0, Δ_2 = −0.7 %, (b) r_2/r_1 = 2.0, W/r_1 = 1.1, Δ_2 = −0.7 %, (c) r_2/r_1 = 2.0, W/r_1 = 1.2, Δ_2 = −0.7 %, (d) r_2/r_1 = 2.0, W/r_1 = 1.3, Δ_2 = −0.7 % [21]. The black solid lines and the black dashed lines represent the values of n_{eff} and A_{eff}, which were simulated based on full-vector FEM [16]. The couple of white dashed and dotted lines correspond to the upper limit of bending loss (*BL*) of the higher-order mode (HOM) at 1530 nm when *R* equals 140 mm and the lower limit of bending loss (*BL*) of the fundamental mode (FM) at 1625 nm when *R* equals 30 mm. To define the single-mode operation, the bending loss of LP_{11}-like HOM should be > 1 dB/m at *R* = 140 mm [36] and we assume the limit value of the bending loss of FM to be 0.5 dB/100 turns at *R* = 30 mm, which is described in ITU-T recommendations G.655 and G.656. Therefore, in order to guarantee the transmission with single-mode operation and low bending loss from C-band to L-band, we only research the field that is surrounded by the couple of white dashed and dotted lines. If we decided the required Δn_{eff} and the target value of A_{eff}, we can choose two non-identical cores with same A_{eff} in such field. The reason why we set the A_{eff} to be the same is that the different A_{eff} in both Hetero-TA-cores will cause splice loss between different groups and different optical signal-to-noise ratio (OSNR) depending on the groups. Therefore, we should be aware of that it is very hard to find three kinds of cores in above-mentioned filed if we want both of cores to reach the same large A_{eff}, such as 100 μm^2. Thus, we choose two kinds of cores for the Hetero-TA-MCF, which answers the question raised at the beginning of this chapter.

If we define the target value of A_{eff} to be 100 μm^2, we can pick four pairs of Hetero-TA-cores at the critical points of the *BL* limit lines that are shown as the filled circles in the Fig. 4.3. Here, we fix r_2/r_1 to be 2.0 and change W/r_1 from 1.0 to 1.3 to investigate how the width of trench region influences the crosstalk between the neighboring cores. We can observe an interesting phenomenon that no matter how W/r_1 changes, the value of n_{eff} and A_{eff} are not influenced to a large extent, but the bending loss of FM and HOM are impacted.

In this part we only try to introduce a core-selecting approach for Hetero-TA-cores theoretically, which is just an example and concept for the selection of cores. The core-selecting field will alter as the location and thickness of trench layer change, so in the following part we will discuss the core-selecting process with different Δ_2 and different design of trench layer.

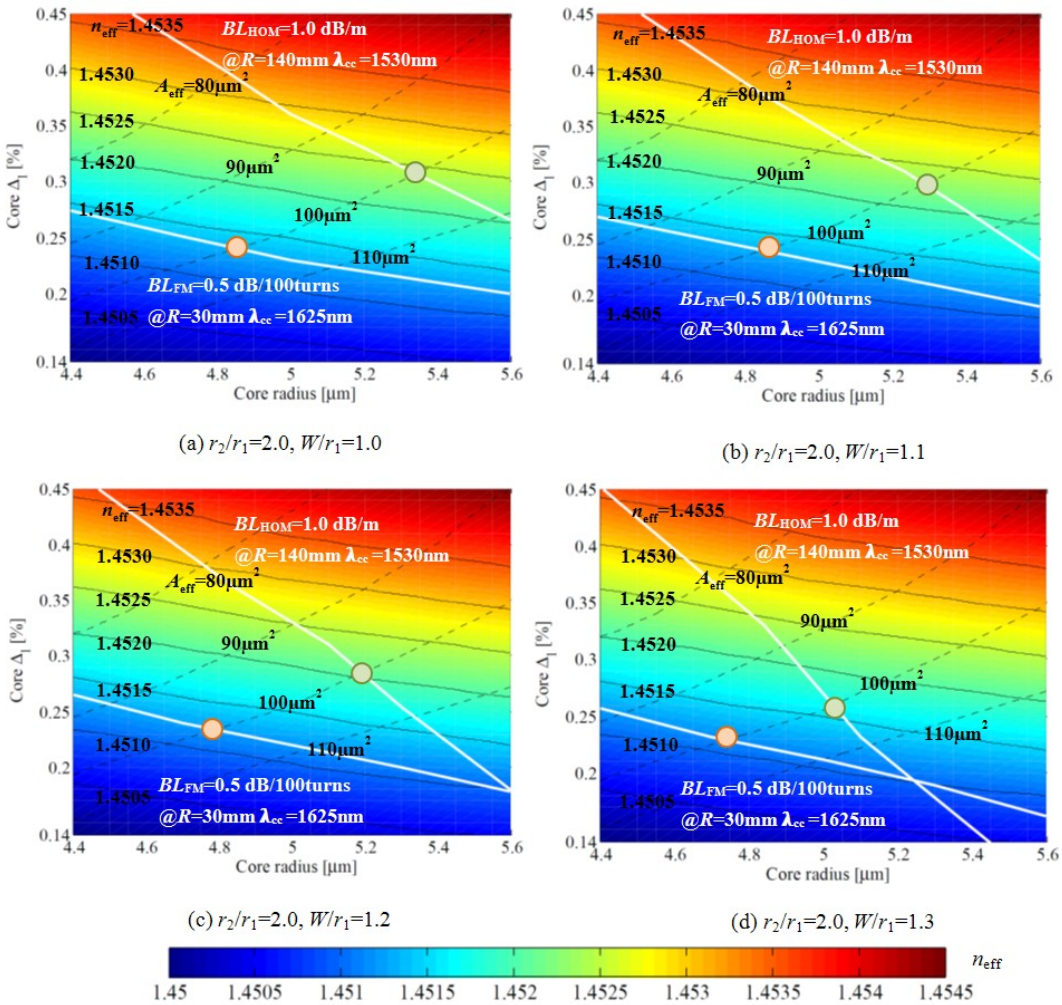

Fig. 4.3 Core effective index and effective area of the fundamental mode at 1550-nm wavelength as function of core radius r_1 and core Δ_1, where (a) r_2/r_1 = 2.0, W/r_1 = 1.0, Δ_2 = −0.7 %, (b) r_2/r_1 = 2.0, W/r_1 = 1.1, Δ_2 = −0.7 %, (c) r_2/r_1 = 2.0, W/r_1 = 1.2, Δ_2 = −0.7 %, (d) r_2/r_1 = 2.0, W/r_1 = 1.3, Δ_2 = −0.7 %.

B. Design of trench layer and Δ_2

In order to find out the optimized arrangement of trench structure, we fixed the thickness of trench and then shift the location of trench layer. Here, we just consider the range that $1.0 \leq r_2/r_1 \leq 2.0$, but it should be noticed that the FEM method can be used to calculate the crosstalk no matter what r_2/r_1 and W/r_1 are. For each set of r_2/r_1 and W/r_1, we can obtain n_{eff} and A_{eff} which correspond to each core r_1 and core Δ_1. And then we can select a pair of cores with the required A_{eff} and Δn_{eff} according to the core-selecting method introduced in the above part. In order to obtain as small R_{pk} and large *RCMF* as possible, we pick two cores with the same A_{eff} at the critical points of upper and lower *BL* limit lines to get Max Δn_{eff} and arrange these two cores very closely to get the Min Λ. Here, we define the minimum required distance between the outer circumferences of trench layer (*d*) to be 2 μm so that the trench does not overlap to each other. Additionally, as shown in Fig. 4.3, if we enlarge the A_{eff} expected, the Max Δn_{eff} we can obtain will decrease, which means that there is a trade-off relationship between Δn_{eff} and A_{eff}, and this kind of trade-off relationship also exists similarly between R_{pk} and A_{eff}. Therefore, in order to evaluate the Hetero-TA-MCF more simply, we fixed the target value of A_{eff} to 100 μm^2 and then analyze the influence of Max Δn_{eff} and Min Λ on R_{pk}, *RCMF* and crosstalk.

Firstly, we analyze how Δ_2, r_2/r_1 and W/r_1 impact Max Δn_{eff} and Min Λ. Fig. 4.4 and Fig. 4.5 illustrate the dependence of Max Δn_{eff} and Min Λ between two adjacent Hetero-TA-cores on r_2/r_1 and W/r_1 with $A_{\mathrm{eff}} = 100$ μm^2 on the conditions that (a) $\Delta_2 = -0.5$ %, (b) $\Delta_2 = -0.7$ % and (c) $\Delta_2 = -0.9$ %, respectively [26]. From Fig. 4.4 and Fig. 4.5, we can observe that as W/r_1 is reduced, Max Δn_{eff} increases and Min Λ decreases and if Δ_2 is set to be much lower, a very small W/r_1 can ensure the large enough Δn_{eff} and the extremely small Λ between two neighboring Hetero-TA-cores. Secondly, we explain how to optimize crosstalk, R_{pk} and *RCMF* through designing Δ_2, r_2/r_1 and W/r_1.

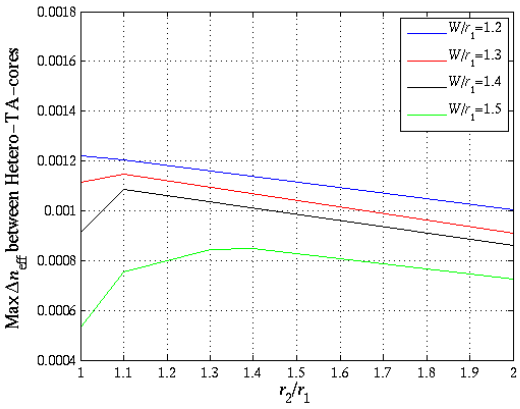

(a) $\Delta_2 = -0.5$ %

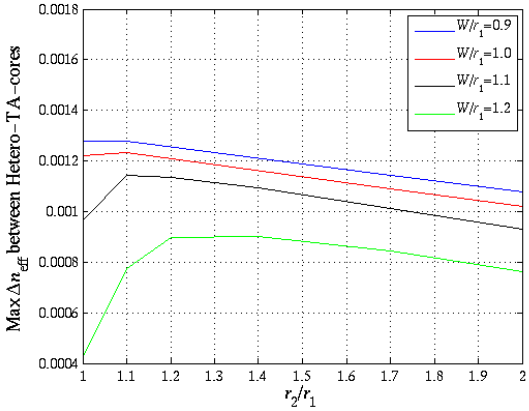

(b) $\Delta_2 = -0.7$ %

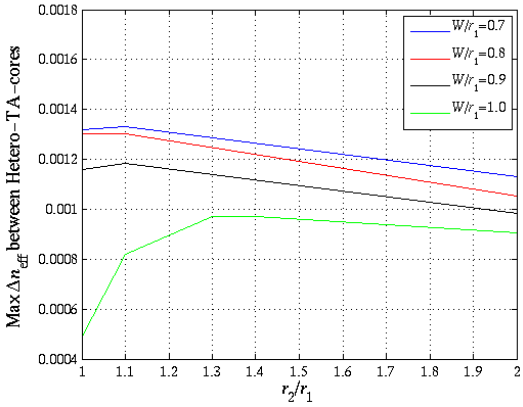

(c) $\Delta_2 = -0.9$ %

Fig. 4.4 Dependence of Max Δn_{eff} between two adjacent Hetero-TA-cores on r_2/r_1 and W/r_1 under the condition that $A_{\mathrm{eff}} = 100\ \mu\mathrm{m}^2$, where (a) $\Delta_2 = -0.5$ %, (b) $\Delta_2 = -0.7$ %, and (c) $\Delta_2 = -0.9$ %.

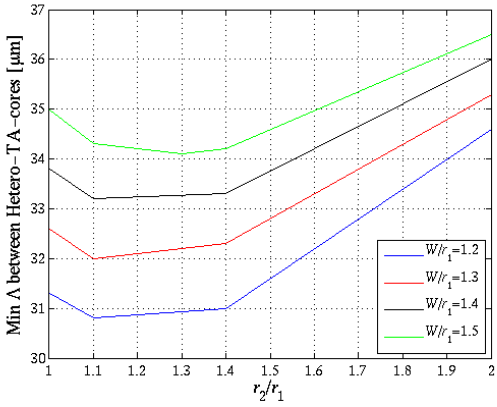

(a) $\Delta 2 = -0.5$ %

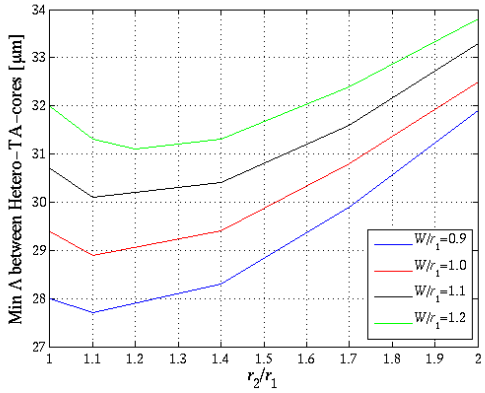

(b) $\Delta 2 = -0.7$ %

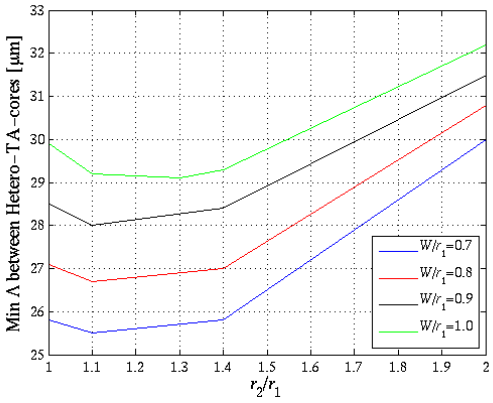

(c) $\Delta_2 = -0.9$ %

Fig. 4.5 Dependence of Min Λ between two adjacent Hetero-TA-cores on r_2/r_1 and W/r_1 under the condition that $A_{eff} = 100\ \mu m^2$, where (a) $\Delta_2 = -0.5$ %, (b) $\Delta_2 = -0.7$ %, and (c) $\Delta_2 = -0.9$ %.

4.3 Optimum scheme of Hetero-TA-MCF

A. Characteristic of crosstalk

As mentioned in last chapter, there are three types of expressions of PCC proposed in [30], which are based on exponential autocorrelation function, Gaussian autocorrelation function, and triangular auto-correlation function, respectively. However, in the non-phase-matching region in which bending radii are larger than R_{pk}, the crosstalk behaviors are not well simulated with a Gaussian autocorrelation function [30]. Moreover, the PCC based on a triangular autocorrelation function cannot be physically acceptable [30]. Thus, as well as the authors in [37], we adopt the PCC based on an exponential autocorrelation function, which is given by

$$h_{pq}(z) = \frac{2K^2{}_{pq}d}{1+(\Delta\beta'_{pq}d)^2}, \tag{4.1}$$

where p, q represent the core p and core q; K_{pq} is the average value of κ_{pq} and κ_{qp}; $\Delta\beta'_{pq}$ is the difference of equivalent propagation constant between core p and core q; d means the correlation length.

In order to avoid numerical solutions of coupled-power equations, we use the average value of PCC over a twist pitch to calculate the crosstalk. The twist pitch referred here is used to represent the unintentional spin or twisting during draw, cabling process, etc. [38] and is assumed to be 5 turns per 100 m. It deserves to be mentioned that however we set the twist pitch, the result of average PCC will not change. In addition, we assume d to be 0.05 m for the calculation of crosstalk, because the d of 0.05-m was proved to agree well with the measurement data in [31]. By using the average PCC and CPT, the crosstalk (XT) between two Hetero-TA-cores with length L is estimated as

$$XT = \tanh(\bar{h}_{pq}L). \tag{4.2}$$

Subsequently, we discuss how to optimize the inter-core crosstalk. When the Hetero-TA-cores are selected, the value of Max Δn_{eff} is decided accordingly. Because crosstalk is determined by mode-coupling coefficient (κ) and Δn_{eff}, we can change Λ to control κ so that required crosstalk can be obtained. As shown in Fig. 4.4, for each set of r_2/r_1 and W/r_1, we can get the Max Δn_{eff} between two Hetero-TA-cores with A_{eff} = 100 μm^2. In

order to analyze the crosstalk, we set an upper limit for Λ that is Λ= 35 μm to ensure R_{pk} does not be too large. And the lower limit of Λ is illustrated in Fig. 4.5. Based on the upper and lower limits of Λ for each set of Hetero-TA-cores, we calculated the maximum and minimum of crosstalk when R = 500 mm after 100-km propagation. The reason why we set the R to be 500 mm is that this bending radius is much larger than the R_{pk}, which means that the crosstalk at R of 500-mm is the one in the bend-insensitive situation.

The range of crosstalk between Hetero-TA-cores for each r_2/r_1 and W/r_1 is shown in Fig. 4.6 [26]. For each r_2/r_1, as W/r_1 increases, crosstalk can be lowered. We can also observe that as Δ_2 is getting smaller, a very small W/r_1 can guarantee the large enough Δn_{eff}, thus the Min Λ is shortened so that the range of crosstalk is enlarged, yet the Max crosstalk becomes the worst.

If we elongate Λ, crosstalk can be lowered, but meanwhile R_{pk} increases and *RCMF* decrease, so crosstalk has a trade-off relationship with R_{pk} and *RCMF*. Hence, in order to optimize the crosstalk, we should balance the value of R_{pk} and *RCMF* at the same time.

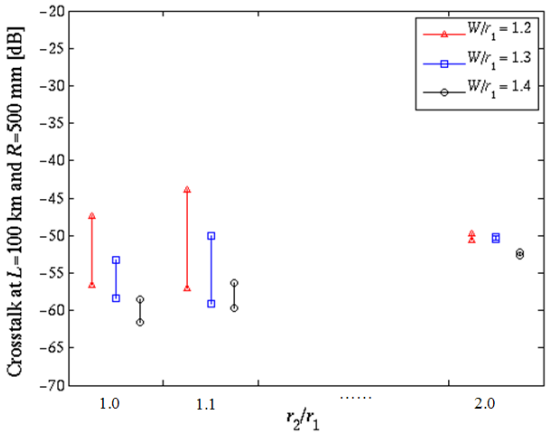

(a) $\Delta 2 = -0.5$ %

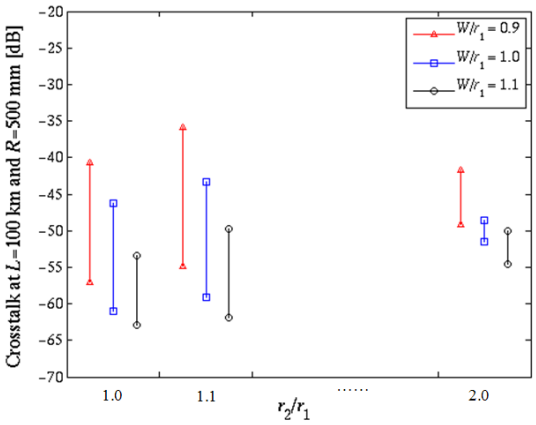

(b) $\Delta 2 = -0.7$ %

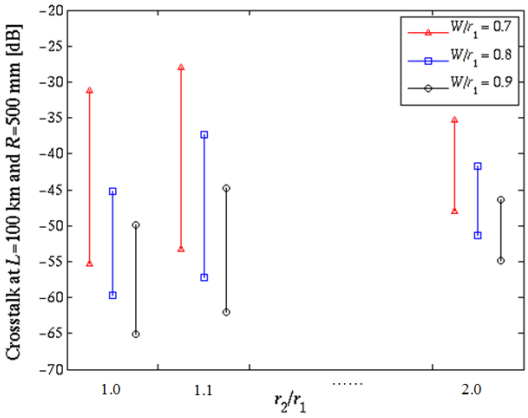

(c) $\Delta_2 = -0.9$ %

Fig. 4.6 Dependence of crosstalk between two adjacent Hetero-TA-cores on r_2/r_1 and W/r_1 under the condition that $A_{\mathrm{eff}} = 100\ \mu\mathrm{m}^2$, where (a) $\Delta_2 = -0.5$ %, (b) $\Delta_2 = -0.7$ %, and (c) $\Delta_2 = -0.9$ %.

B. Characteristic of threshold bending radius (R_{pk})

As shown in Fig. 4.7, when the fiber is under bent condition, we can use the equivalent index model [14] to represent the bent fiber as a corresponding straight one, whose equivalent refractive-index profile can be expressed as

$$n_{\mathrm{eq}}(r,\theta,R) = n(r,\theta)(1+\frac{r}{R}\cos\theta), \tag{4.3}$$

where r is distance from the center of a core to a reference point, and θ is an angle from the radial direction of the bend. For the Hetero-TA-MCF with ring layout, the difference of equivalent propagation-constant ($\Delta\beta'_{mn}$) can be written as

$$\Delta\beta'_{mn} = \Delta\beta_{mn} + \frac{D}{R}\left[\beta_m \cos\theta_1\left(z'\right) - \beta_n \cos\theta_n\left(z'\right)\right], \tag{4.4}$$

where D means the distance between the centers of core and fiber (here, we set the center of the fiber as the reference point), β_m, β_n are the propagation-constant of core m and n before fiber getting bent and

$$\theta_n(z) = \gamma z + \theta_c + (n-1)\frac{2\pi}{N_{core}}. \tag{4.5}$$

θ_n is the angle of a line segment connecting core n and the center of fiber in the radial direction. γ, θ_c, n, and N_{core} stand for a twist rate of the fiber, an offset of the twist, the serial number of core and the core number, respectively.

If we set δn_{eff} to be zero, an extreme value of R called R_{pk} in [14] can be obtained, which can be derived as

$$R_{\mathrm{pk}} = \frac{D\left[n_{\mathrm{eff}\,n}\cos\theta_n(z) - n_{\mathrm{eff}\,1}\cos\theta_1(z)\right]}{n_{\mathrm{eff}\,1} - n_{\mathrm{eff}\,n}}. \tag{4.6}$$

From the expression above, it can be concluded that R_{pk} varies inversely with the difference of n_{eff} (Δn_{eff}) and after fixing Δn_{eff} and D, the corresponding R_{pk} can be determined. Here, Δn_{eff} is the difference of n_{eff} under the straight condition of fiber and is not identical to

δn_{eff} which is the difference of n_{eff} in the bent condition of fiber. From Fig. 4.8 which indicates the dependence of R_{pk} on core pith for each Δn_{eff}, we can know that if we want to reach an R_{pk} smaller than 50 mm, Λ should be smaller than 35 μm and Δn_{eff} value should be larger than 0.001.

Then, we can optimize R_{pk} by analyzing the impact of arrangement of trench layer and the different design of Δ_2. After we fix the location of trench, we can shrink the thickness of the trench layer and lower the Δ_2 to obtain smaller R_{pk} and larger *RCMF*. For each Δ_2, as W/r_1 is enlarged, the Max Δn_{eff} decreases and Min Λ increases so that the R_{pk} becomes larger. This phenomenon can be explained more clearly in Fig. 4.9 [26], which illustrates the dependence of Min R_{pk} on r_2/r_1 and W/r_1 under the condition A_{eff} = 100 μm^2 with three situations of Δ_2. Therefore, after making sure a low crosstalk, we should decrease r_2/r_1 and W/r_1 to get a relative optimized R_{pk}.

In order to understand what the R_{pk} is, we use the four pairs of selected core in Fig. 4.3 for example. In Fig. 4.3 (a), one of the cores has a radius of 5.34 μm and Δ_1 = 0.304% and another core has a radius of 4.86 μm and Δ_1 = 0.242%. In Fig. 4.3 (b), one of the cores has a radius of 5.27 μm and Δ_1 = 0.293% and another core has a radius of 4.83 μm and Δ_1 = 0.239%. In Fig. 4.3 (c), one of the cores has a radius of 5.18 μm and Δ_1 = 0.280% and another core has a radius of 4.77 μm and Δ_1 = 0.234%. In Fig. 4.3 (d), one of the cores has a radius of 5.03 μm and Δ_1 = 0.263% and another core has a radius of 4.75 μm and Δ_1 = 0.240%. Furthermore, in order to make sure the trench not overlap to each other, we defined D_{tr} to be not smaller than 2 μm. Under this requirement, we set each required Λ. The optical properties of the cores in each condition are summarized in Tab. 4.1.

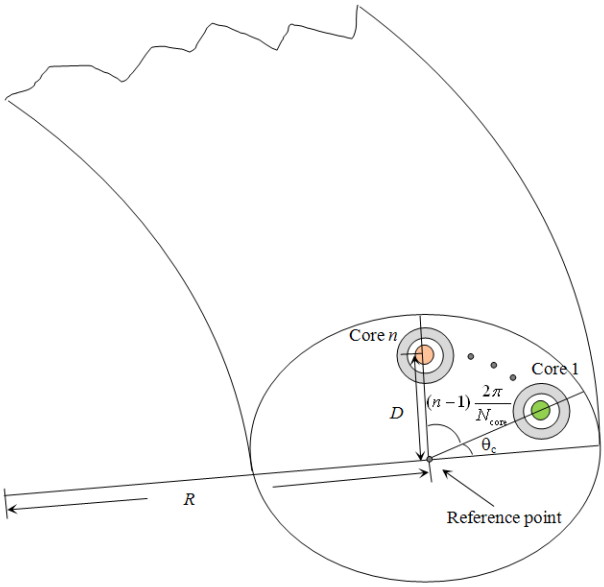

Fig. 4.7 The partial enlarged view of bent Hetero-TA-MCF.

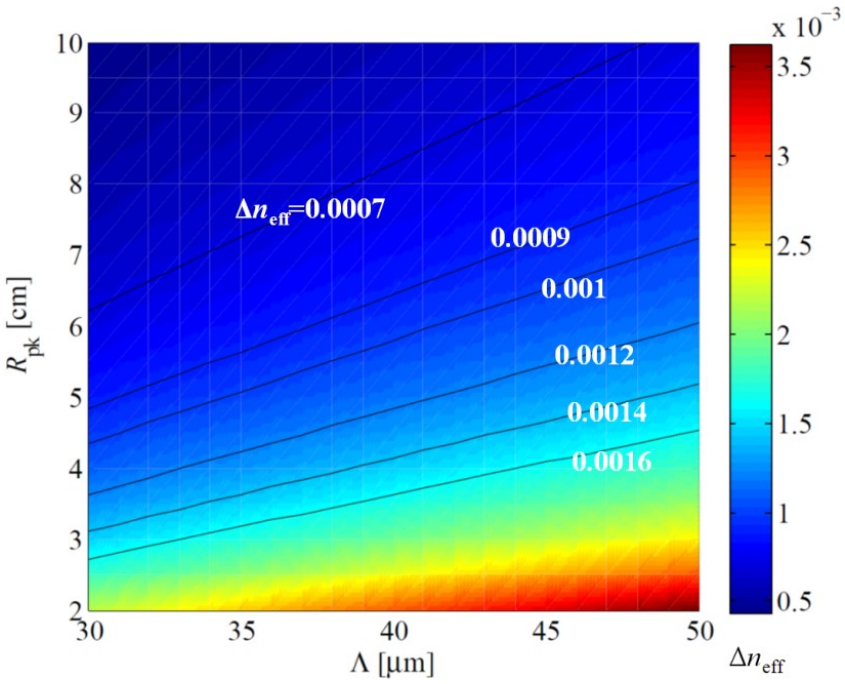

Fig. 4.8 Required Δn_{eff} as function of the Λ and R_{pk}.

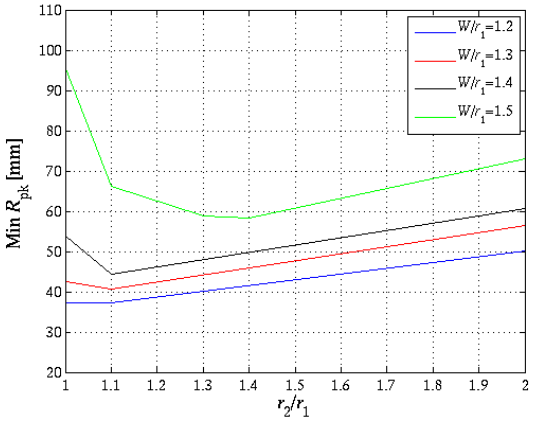

(a) $\Delta 2 = -0.5$ %

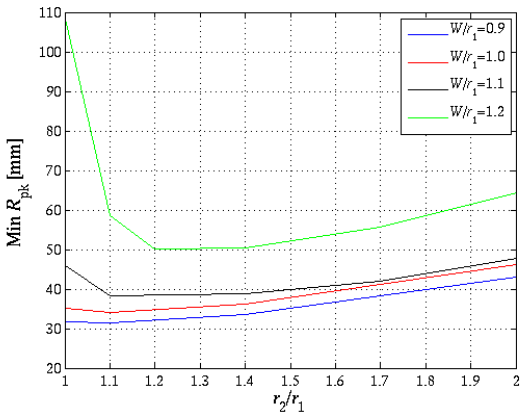

(b) $\Delta 2 = -0.7$ %

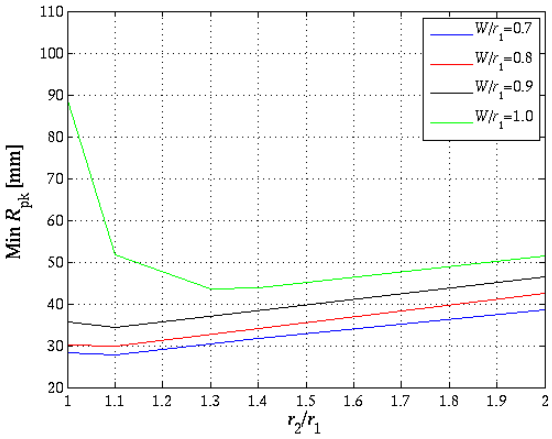

(c) $\Delta_2 = -0.9$ %

Fig. 4.9 Dependence of Min R_{pk} on r_2/r_1 and W/r_1 under the condition that A_{eff} = 100 μm^2, where (a) $\Delta_2 = -0.5$ %, (b) $\Delta_2 = -0.7$ %, and (c) $\Delta_2 = -0.9$ %.

Fig. 4.10 shows the crosstalk of the Hetero-TA-12-core fiber at 100-km propagation as function of bending radius under the four kinds of conditions mentioned above [21]. We can find that once bending radius becomes larger than R_{pk}, the crosstalk of Hetero-MCF decreases immediately after bending radius (R) reaching a critical value R_{pk} and then it converges to a certain value no matter how R increases.

Fig. 4.11 illustrates the crosstalk of the Homo-TA-12-core fiber at 100-km propagation as function of bending radius under same four conditions [21]. The Homo-TA-12-core fiber mentioned here has the same ring structure with the Hetero-TA-12-core fiber and we choose four sorts of cores for the Homo-TA-12-core fiber under these four conditions. In order to compare the crosstalk characteristics of the Homo-TA-12-core fiber with that of the Hetero-TA-12-core fiber, we assume these four kinds of cores to have the same core parameters with the first kind of core in each condition of the Hetero-TA-12-core fiber that we described above. For the condition (a), r_1 = 5.34 μm, Δ_1 = 0.304%, and Λ = 33 μm. For condition (b), r_1 = 5.27 μm, Δ_1 = 0.293%, and Λ = 34 μm. For condition (c), r_1 = 5.18 μm, Δ_1 = 0.280%, and Λ = 34 μm. And for condition (d), r_1 = 5.03 μm, Δ_1 = 0.263%, and Λ = 35 μm. We can find obviously that the crosstalk of the Homo-TA-MCF become larger and larger as increasing the bending radius. Therefore, we can see the merit of Hetero-TA-MCF clearly from this comparison.

Table 4.1 The optical properties of the cores in different conditions (1550 nm)

Item	A_{eff}	Δn_{eff}	Λ	CD
Unit	μm^2	-	μm	μm
r_2/r_1 = 2.0, W/r_1 = 1.0	100	0.001	33	201.5
r_2/r_1 = 2.0, W/r_1 = 1.1	100	0.0009	34	205.4
r_2/r_1 = 2.0, W/r_1 = 1.2	100	0.0007	34	205.4
r_2/r_1 = 2.0, W/r_1 = 1.3	100	0.0005	35	209.2

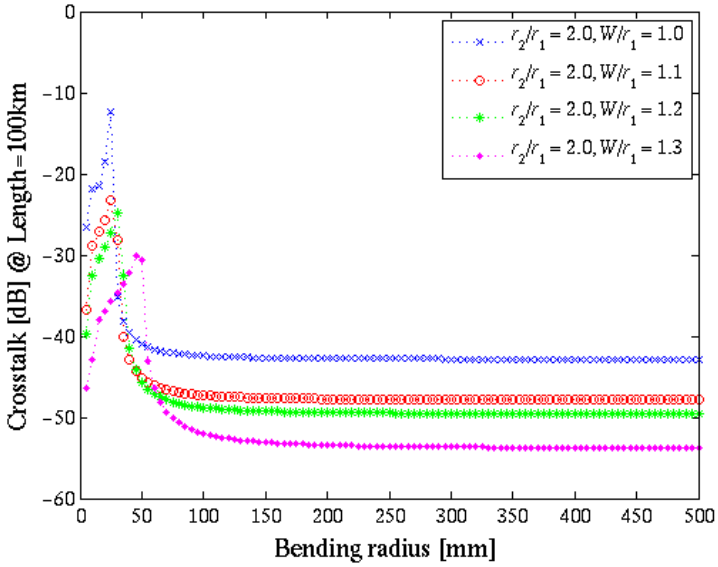

Fig. 4.10 Crosstalk of Hetero-TA-12-core fiber at 100-km propagation as function of bending radius.

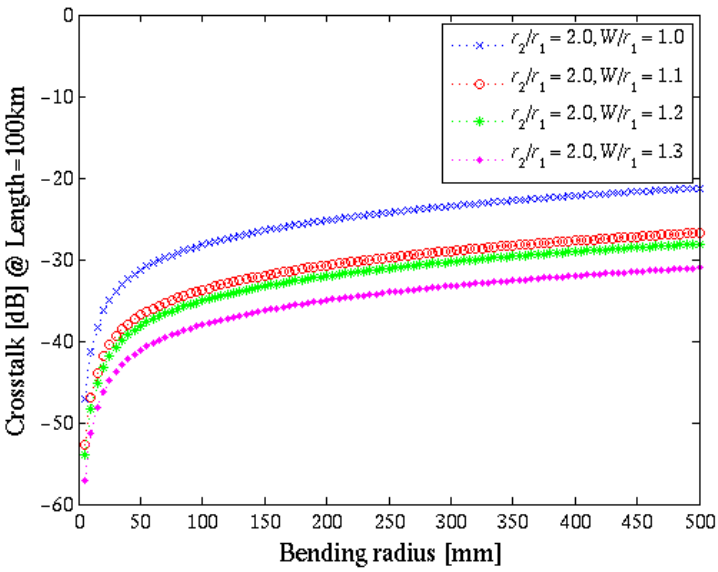

Fig. 4.11 Crosstalk of Homo-TA-12-core fiber at 100-km propagation as function of bending radius.

C. Characteristic of relative core multiplicity factors (RCMF)

There is a concept proposed in [15] called core multiplicity factor (*CMF*), which is defined to compare the core density of MCFs. The *CMF* is given by

$$CMF = \frac{N_{core}\ A_{eff}}{\pi\left(CD/2\right)^2}, \tag{4.7}$$

where N_{core} and *CD* represent number of core and cladding diameter respectively.

RCMF is a ratio between *CMF* of a MCF and a standard single core single mode fiber with $A_{\text{eff}} = 80\ \mu\text{m}^2$ at 1550 nm and $CD = 125\ \mu\text{m}$, which is shown as

$$RCMF = \frac{N_{core}\ A_{eff}}{\pi(CD/2)^2} \Big/ \frac{80}{\pi(125/2)^2}. \tag{4.8}$$

The maximum *RCMF* of the Homo-seven-core fiber is estimated to be 6.0 [39], thus we can treat 6.0 to be one of the design indices of the Hetero-TA-MCF model.

As the core number and core pitch of Hetero-TA-MCF are fixed, the cladding diameter (*CD*) can also be determined correspondingly. As shown in Fig. 4.12, the expression of *CD* can be written as

$$CD = \frac{\Lambda}{\sin(\frac{\pi}{N_{core}})} + 2OCT, \tag{4.9}$$

where *OCT* is the abbreviation of outer cladding thickness. In order to reduce the micro-bending loss, the *OCT* has different required minimum value corresponding to the different A_{eff}. If we expect the A_{eff} to reach 110 μm^2 [15] or 80 μm^2 [14], the *OCT* needs to be at least 40 μm or 30 μm, respectively. Based on the linear relationship of A_{eff} and *OCT*, we can obtain the required value of *OCT* under any A_{eff} conditions. In addition, if we want to decrease the failure probability of a fiber in order to guarantee the mechanical reliability, *CD* should not be larger than 225 μm [40]. If we set the goal value of A_{eff} to be 100 μm^2, the *OCT* should be at least 37 μm and in this case the dependence of *CD* on the Λ is shown as Fig. 4.13. From Fig. 4.13, we can observe that core number of 14 is the upper limit with $\Lambda \approx 33\ \mu\text{m}$ since *CD* cannot beyond 225 μm.

And then we continue to analyze the relationship between *RCMF* and N_{core}. After

substituting the *CD* in Eq. (4.8) by Eq. (4.9), *RCMF* can be rewritten as

$$RCMF = \frac{N_{core}\ A_{eff}}{\pi[(\Lambda / \sin\left(\frac{\pi}{N_{\text{core}}}\right) + 2OCT) / 2]^2} / \frac{80}{\pi(125/2)^2}. \tag{4.10}$$

Fig. 4.14 shows the dependence of Max *RCMF* on r_2/r_1 and W/r_1 with $A_{\text{eff}} = 100\ \mu\text{m}^2$ and N_{core} =14 on the conditions that (a) $\Delta_2 = -0.5$ %, (b) $\Delta_2 = -0.7$ % and (c) $\Delta_2 = -0.9$ %, respectively [26]. It is obvious that when we decrease r_2/r_1, W/r_1 and lower Δ_2, the *RCMF* can be optimized.

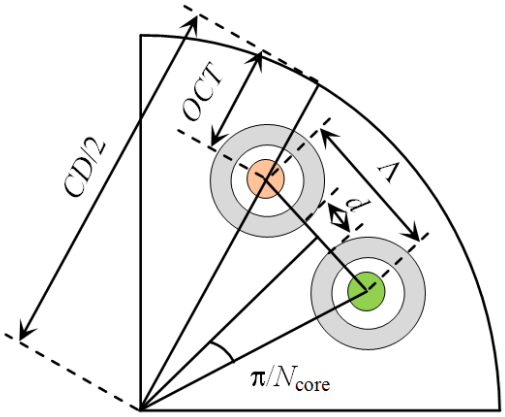

Fig. 4.12 Partial enlarged view of Hetero-TA-MCF.

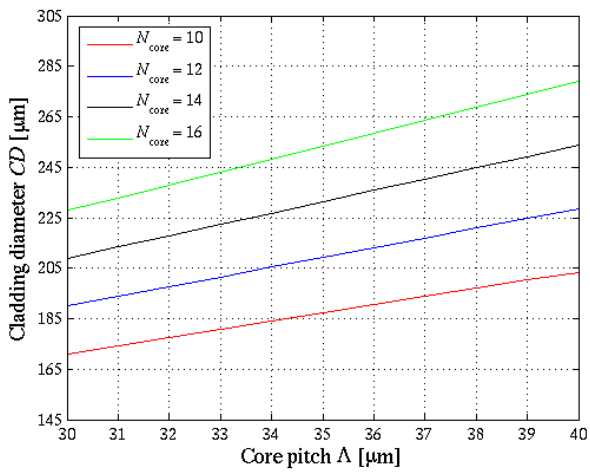

Fig. 4.13 Dependence of cladding diameter on core pitch when $A_{\text{eff}} = 100\ \mu\text{m}^2$.

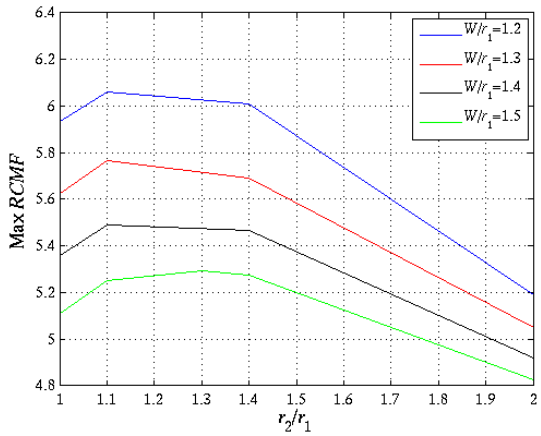

(a) $\Delta 2 = -0.5$ %

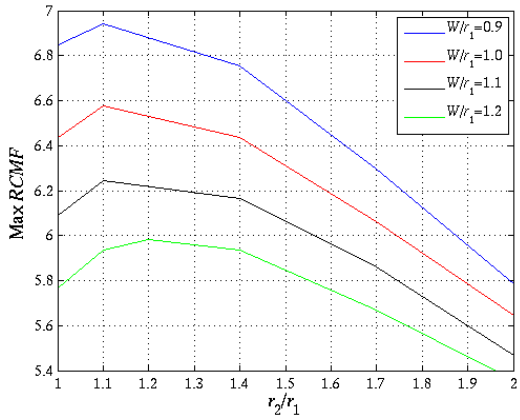

(b) $\Delta 2 = -0.7$ %

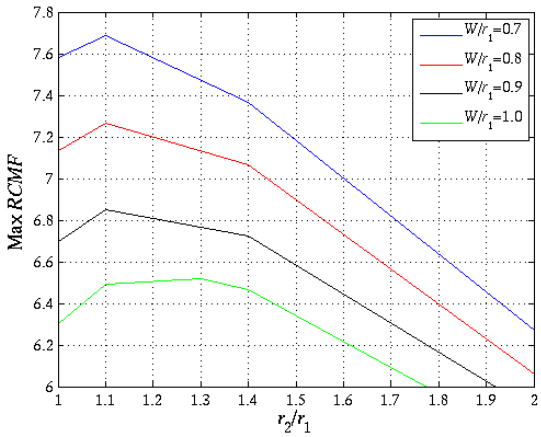

(c) $\Delta_2 = -0.9$ %

Fig. 4.14 Dependence of Max *RCMF* on r_2/r_1 and W/r_1 under the condition that $A_{eff} = 100\ \mu m^2$ and $N_{core} = 14$, where (a) $\Delta_2 = -0.5$ %, (b) $\Delta_2 = -0.7$ %, and (c) $\Delta_2 = -0.9$ %.

After analyzing how the variables r_2/r_1, W/r_1 and Δ_2 impact the crosstalk, R_{pk}, and *RCMF*, we propose two sets of relative optimized parameters for Hetero-TA-14-core fiber, based on different requirements. Here, only if we make sure the $\Lambda \leq 33$ μm, we are allowed to arrange 14 cores inside the fiber.

In the first case, we aim at an extremely small R_{pk} which need to be around 30 mm. So we should decrease r_2/r_1 and W/r_1 as much as possible, but at same time we should also control crosstalk to be an acceptable value, therefore we choose appropriate parameters for r_2/r_1 and W/r_1, which are shown in Tab. 4.2.

In the second case, our target is to obtain a very low crosstalk which should be −50 dB/100 km or so. Here, we set Δ_2 to be −0.7 % and make W/r_1 as large as possible under the requirement of the Δn_{eff}. After balancing every design parameter, we decide the value for each variable, which are summarized in Tab. 4.2.

Table 4.2 Relative Optimized design parameters for Hetero-TA-14-core fiber

Item	Δ_2	r_2/r_1	W/r_1	Λ	Δn_{eff}	*XT*	R_{pk}	*RCMF*	A_{eff}
Unit	%	-	-	μm	-	dB/100 km	mm	-	μm^2
Case #1	−0.9	1.4	0.7	26.4	0.0012	−28.4	31.7	7.37	100
Case #2	−0.7	1.4	1.1	30.4	0.0011	−49.6	41.9	6.16	100

4.4 Conclusion

In this chapter, we firstly introduced the selection method for two trench-assisted non-identical cores after considering the bending loss, required A_{eff} and Δn_{eff}. We presented four types of color map to show the core selecting process with W/r_1 equaling 1.0, 1.1, 1.2, and 1.3 respectively. From the color map, we can conclude that the change of W/r_1 does not impact the value of A_{eff} and n_{eff}, but influences the bending loss. Secondly, we analyzed the optimization method of crosstalk, R_{pk} and *RCMF* by discussing different design of r_2/r_1, W/r_1 and Δ_2.

As described in section 4.3, these three optimized objects cannot reach the optimized value at the same time, because there is trade-off relationship among them. According to different demand of design, we proposed two kinds of relative optimized design schemes for Hetero-TA-14-core fiber. In the first case, we achieve a very small R_{pk} of about 31.7 mm, and a large *RCMF* of 7.37 by sacrificing the crosstalk which is −28.4 dB/100 km. In the second case, the crosstalk is much lower which can reach about −50 dB/100 km, R_{pk} is 41.9 mm, and *RCMF* is 6.16.

Chapter 5 Design and analysis of one-ring layout heterogeneous trench-assisted few-mode multi-core fiber (Hetero-TA-FM-MCF) with low differential mode delay and large effective area

5.1 Introduction

Several multiplexing technologies such as space-division multiplexing (SDM) using multi-core fiber (MCF) [41] and mode-division multiplexing (MDM) using few-mode fiber (FMF) [9] are being intensively investigated to overcome the capacity limit of the network traffic in the current conventional optical communication systems. In order to further increase the transmission capacity, the combination design of multi-core and few-mode has been discussed recently [12, 13].

For FMF, multiple-input-multiple-output (MIMO) digital signal processing (DSP) is applied to recover the transmitted signals. In order to decrease the MIMO-DSP complexity, we should guarantee as low differential mode delay (DMD) over C+L bands as possible. FMF with low DMD is of benefit to MDM transmission utilizing MIMO. Furthermore, low DMD in the wide wavelength region is required for the wavelength division multiplexing (WDM) transmission applications [10]. To realize low DMD, the 1st approach is using complex refractive index profile, such as multi-step index profile [42], graded index [43], and graded index profile with trench (T-GIP) [44], to add more degree of freedom to control the value of DMD. FMFs with T-GIP have realized ultra-low DMD less than 36 ps/km over the C band [44]. The 2nd approach that realizes low DMD over the wide band is called DMD managed transmission line technique [10, 45]. The line consists of two kinds of FMFs with positive and negative DMDs to compensate for the total DMD. A transmission line which realizes low DMD within |3| ps/km over C band and L band has been proposed [46].

In this chapter, we investigate and analyze appropriate index profile for few-mode core that support two LP modes respectively and then propose a relative optimum design scheme for heterogeneous trench-assisted FM-MCF (Hetero-TA-FM-MCF) with low DMD and large effective area. Additionally, in this work, trench layer is deployed around each core to realize low inter-core crosstalk even with small core pitch and heterogeneous cores is chosen to make

the fiber insensitive to the curvature of fiber, which are explained in more detail in our last works [21, 26].

5.2 Design method of Hetero-TA-FM-MCF

A. Profile of trench-assisted multi-step index few-mode core (TA-MSI-FMC)

We design trench-assisted few-mode core (TA-FMC) with two kinds of modes — LP_{01} mode and LP_{11} mode. Besides the number of mode transmitting in the core, we should also take into account the inter-mode crosstalk and the differential mode delay (DMD) [47]. For a step index profile, it is impossible to design a fiber with low DMD over a transmission band like C and L bands due to its simple profile. Nevertheless, the multi-step index (MSI) profile that is shown as Fig. 5.1 [48] has more degree of freedom to control the difference of group delays between LP_{01} mode and LP_{11} mode, since the DMD characteristics are sensitive to the change of the refractive index profile. In Fig. 5.1, a_1, r_1, r_2, W, Δ_1, Δ_2 and Δ_t stand for inner core radius, outer core radius, the distance between the center of inner core and the inner circumference of trench, the thickness of the trench layer, the relative refractive-index difference between inner core and cladding, the relative refractive-index difference between outer core and cladding, and the relative refractive-index difference between trench and cladding, respectively. In the following subsections, we analyze and discuss the relationship between these parameters and DMD and find out the appropriate set of a_1, Δ_1, r_1/a_1, Δ_d, r_2/r_1, W/r_1, and Δ_t to obtain a couple of TA-MSI-FMCs with low DMD, low DMD slope, small inter-core crosstalk, and large effective area (A_{eff}).

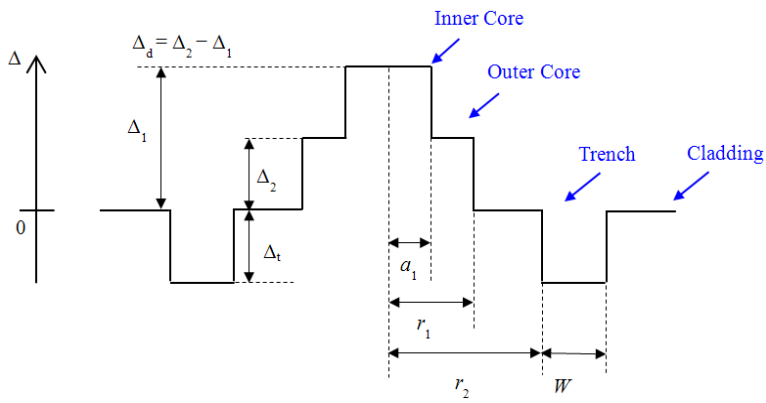

Fig. 5.1 Refractive index profiles of TA-MSI-FMCs.

B. TA-MSI-FMC with low DMD and low DMD slope

We define the DMD as a value obtained by subtracting the mode group delay of the fundamental mode (τ_{LP01}) from that of the higher-order mode (τ_{LP11}) and the expression of DMD is written as follows.

$$DMD = \tau_{LP11} - \tau_{LP01} = \frac{n_{eff\,11} - n_{eff\,01}}{c} - \frac{\lambda}{c}\left(\frac{\partial n_{eff\,11}}{\partial \lambda} - \frac{\partial n_{eff\,01}}{\partial \lambda}\right), \tag{5.1}$$

where c is the light velocity in a vacuum, n_{eff} is the effective index, and λ means free space wavelength. Since we should also ensure the low DMD over C+L bands transmission, we need to design two kinds of TA-MSI-FMCs with not only low DMD at a certain operating wavelength but also low DMD slope for the wavelength (λ).

Fig 5.2 shows DMD and DMD slope as function of r_2/r_1 at λ = 1550 nm. Here, we fixed the value for a_1, Δ_1, r_1/a_1, Δ_d, W/r_1, and Δ_t, which are assumed as 3.6 μm, 0.5 %, 2.0, −0.13 %, 1.0, and −0.7 %, respectively [48]. From Fig. 5.2, we can know that the location of trench layer has a big impact on the DMD and DMD slope. Furthermore, we can also observe that as r_2/r_1 increases, DMD and DMD slope are getting smaller and when r_2/r_1 = 1.6, the absolute value of DMD slope for λ=1550 nm is the smallest and approximates to 0 ns/km/nm.

Fig. 5.3 illustrates DMD and DMD slope as function of r_1/a_1 and Δ_d at λ=1550 nm. Here, we assumed a_1, Δ_1, r_2/r_1, W/r_1, and Δ_t to be 3.6 μm, 0.5 %, 1.6, 1.0, and −0.7 %, respectively [48]. In Fig. 5.3, we can see that when we fix Δ_d and shift r_1/a_1, DMD does not change flexibly but DMD slope alters slowly. On the contrary, if we fix r_1/a_1 and shift Δ_d, DMD changes flexibly and DMD slope also alters slowly. The above-mentioned two approaches can both make DMD slope change, but only the second approach can help us control the DMD over the wide band. When r_1/a_1 is fixed, we can compensate the increment and decrement of DMD and DMD slope caused by altering r_2/r_1 via changing the value of Δ_d. This phenomenon implies that we can keep a suitable value for r_1/a_1 at first and then take advantage of both r_2/r_1 and Δ_d to find a reference point with relative low DMD and DMD slope. If we set r_1/a_1 to be 2.0, the Δ_d can be shifted from −0.17 % to −0.11 % so that the approximate range of DMD slope is $-2\times10^{-4} \sim +2.7\times10^{-4}$ ns/km/nm and that of DMD is −1 ~ +1 ns/km. It indicts that r_1/a_1 of 2.0 is an appropriate design value, which make it possible for us to find suitable a_1, Δ_1 for inner core nearby the reference point — a_1 of 3.6 μm and Δ_1 of 0.5 % to obtain both low absolute DMD and DMD slope under the condition that r_2/r_1 = 1.6 and Δ_d = −0.13 %. Here, we do not analyze the impact of W/r_1 and Δ_t on the DMD, which will be discussed in the following subsection.

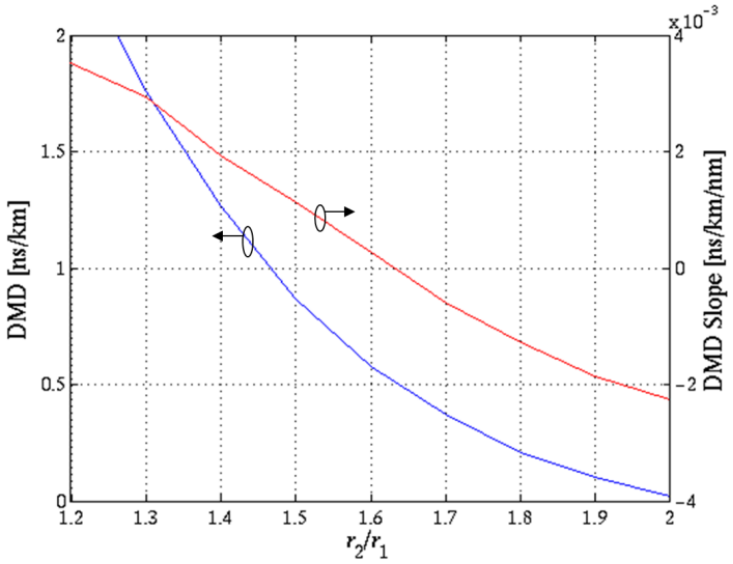

Fig. 5.2 DMD and DMD slope as function of r_2/r_1 at λ=1550 nm when a_1 = 3.6 μm, Δ_1 = 0.5 %, r_1/a_1 = 2.0, Δ_d = −0.13 %, W/r_1 = 1.0, and Δ_t = −0.7 %.

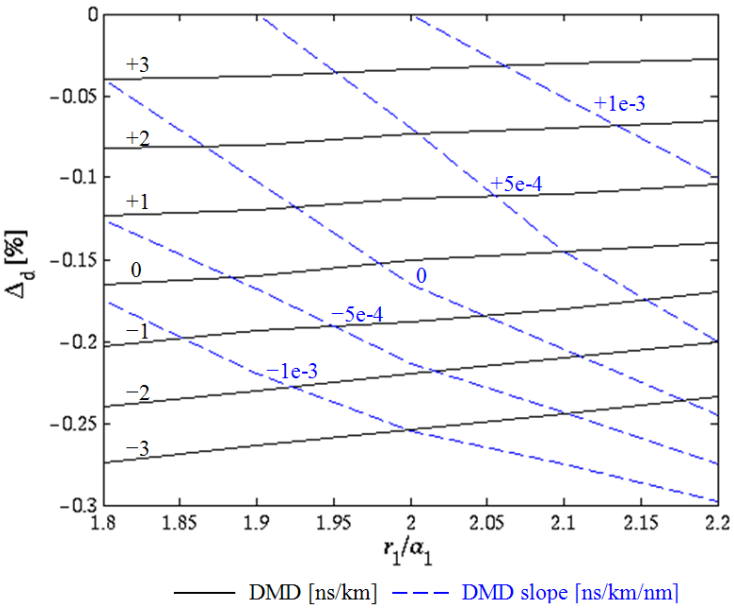

Fig. 5.3 DMD and DMD slope as function of r_1/a_1 and Δ_d at λ=1550 nm when a_1 = 3.6 μm, Δ_1 = 0.5 %, r_2/r_1 = 1.6, W/r_1 = 1.0, and Δ_t = −0.7 %.

Figure 5.4 shows DMD at λ=1550 nm as function of a_1 and Δ_1 when r_2/r_1 = 1.6 and Δ_d = −0.13 % [48]. Here, we fixed the value for r_1/a_1, W/r_1, and Δ_t, which are assumed as 2.0, 1.0, and −0.7 %, respectively. Because different effective area (A_{eff}) in both cores will cause splice loss between different groups and different optical signal-to-noise ratio (OSNR) depending on the groups. In this work, we design two kinds of TA-MSI-FMCs, and it is very hard to ensure the A_{eff} of LP_{01} mode and LP_{11} mode to be the same in these two cores. Therefore in order to decrease such splice loss and OSNR as far as possible, we require the same A_{eff} of LP_{01} mode in both cores. Hence, we define the target value of A_{eff} of LP_{01} mode (A_{eff_LP01}) in both TA-MSI-FMCs to be 110 μm^2. Through investigation we find that when Δ_d is around −0.13 % under the condition that r_2/r_1 is 1.6, it is possible to find a_1 and Δ_1 which can obtain A_{eff_LP01} of 110 μm^2 and achieve low absolute value of DMD as well. In the Fig. 5.4, the black solid line and black dash line represent A_{eff_LP01} and effective index of LP_{01} mode (n_{eff_LP01}), which are both simulated based on full-vector FEM [16]. The upper and lower white solid lines represent the cutoff of LP_{21} mode and the limit of LP_{11} mode at W/r_1 of 0.2. The upper and lower white dash lines stand for the cutoff of LP_{21} mode and the limit of LP_{11} mode at W/r_1 of 0.8. It should be noticed that the change of W/r_1 will not influence the value of n_{eff} and A_{eff} to a large extent but the two-mode operation region will shift as W/r_1 alters. We set W/r_1 to be 0.8 and 0.2 in order to make it probable to choose two sorts of TA-MSI-FMCs with same A_{eff_LP01} of 110 μm^2, low DMD and relative large difference between n_{eff_LP01} in two TA-MSI-FMCs (Δn_{eff_LP01}). Here, to define the two-mode operation, the bending loss (*BL*) of LP_{21}-like HOM should be > 1 dB/m at R = 140 mm, which is similar to the definition of *BL* of LP_{11}-like HOM in [36] and we assume the limit value of the *BL* of LP_{11}-like HOM to be 0.5 dB/100 turns at R = 30 mm, according to the description of *BL* of fundamental mode in ITU-T recommendations G.655 and G.656. To ensure a relative small R_{pk} which is a critical value of bending radius [14], we define the required Δn_{eff_LP01} to be about 0.0008. In this case, we can select two kinds of TA-MSI-FMCs with low DMD and DMD slope in the two-mode operation regions, which are shown as the filled circles in red and green in Fig. 5.4. For the filled circles in red which is designated as core 1, a_1 = 3.81 μm, Δ_1 = 0.406 %, DMD at λ of 1550 nm is –160.90 ps/km and DMD slope at λ of 1550 nm is 0.27 ps/km/nm; For the filled circles in green which is designated as core 2, a_1 = 3.92 μm and Δ_1 = 0.458 %, DMD at λ of 1550 nm is 168.30 ps/km and DMD slope at λ of 1550 nm is –0.27 ps/km/nm.

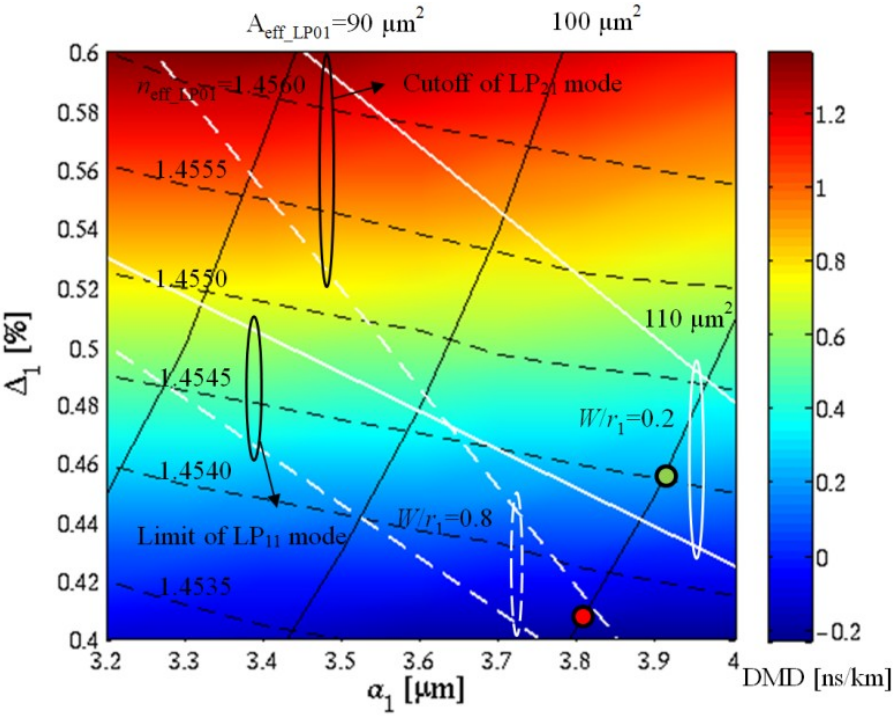

Fig. 5.4 DMD at λ of 1550 nm as function of a_1 and Δ_1 when r_2/r_1 = 1.6, Δ_d = −0.13 %, r_1/a_1 = 2.0, W/r_1 = 1.0, and Δ_t = −0.7 %.

5.3 Optimum scheme of Hetero-TA-FM-MCF

A. Optimal TA-MSI-FMC

In order to get the optimum scheme of TA-MSI-FMC, we should analyze the impact of each parameter to DMD at first. To begin with, we discuss the impact of r_2/r_1 and Δ_d on the DMD and DMD slope. As shown in Fig. 5.2, as r_2/r_1 shifts, DMD will decrease or increase. So in order to compensate for the decreased or increased DMD, we can find the solution in Fig. 5.3 that to alter the absolute Δ_d, which means that we can change r_2/r_1 and Δ_d to control the DMD. We analyzed and obtained the appropriate Δ_d for different r_2/r_1 that (a) r_2/r_1 = 1.3, Δ_d = −0.16 %, (b) r_2/r_1 = 1.4, Δ_d = −0.15 %, (c) r_2/r_1 = 1.5, Δ_d = −0.14 %, (d) r_2/r_1 = 1.6, Δ_d = −0.13 %, (e) r_2/r_1 = 1.7, Δ_d = −0.12 %, (f) r_2/r_1 = 1.8, Δ_d = −0.11%. Fig. 5.5 shows DMD at λ=1550 nm as function of a_1 and Δ_1 under these six situations [48]. Here, we still assume r_1/a_1 to be 2.0 since in this case Δ_d that shifts within −0.17 % ~ −0.11 % can guarantee the low absolute DMD and DMD slope. Moreover, we fixed W/r_1 to be 1.0 and Δ_t to be −0.7 % to simulate the DMD for the above-mentioned six situations. We also define the target A_{eff_LP01}

and $\Delta n_{\text{eff\_LP01}}$ to be 110 μm^2 and about 0.0008, and then we pick up six pairs of TA-MSI-FMCs with low DMD which are corresponding to the filled circles in Fig. 5.5. Fig. 5.6 illustrates the wavelength dependence of DMD for these six couple of TA-MSI-FMCs [48]. In Fig. 5.6, we can observe that as r_2/r_1 increases, the DMD slope is getting smaller and when it equals 1.6, the DMD slope is almost 0 ns/km/nm. Furthermore, when r_2/r_1 increases, the difference between the DMD in both cores becomes larger.

Subsequently, we analyze the impact of W/r_1 and Δ_t on the DMD and DMD slope. Here, we fixed the value for a_1, Δ_1, r_1/a_1 that are 3.6 μm, 0.5 %, 2.0, respectively. Figures 5.7(a) and 5.7(b) show DMD and DMD slope dependence on W/r_1 [48]. In Fig. 5.7(a) and Fig. 5.7(b), we can see that adjusting W/r_1 is another way to control DMD and DMD slope, but when W/r_1 becomes lager than ~0.5, it will not affect the DMD and DMD slope any more. Moreover, as r_2/r_1 increase, W/r_1 has less impact on the DMD and DMD slope, which means that when the trench layer is deployed far away from the outer core, the thickness of trench will not influence the value of DMD and DMD slope. Figures 5.8(a) and 5.8(b) show DMD and DMD slope dependence on Δ_t [48]. In Fig. 5.8(a), we can also observe a similar phenomenon that when r_2/r_1 is getting larger, the impact of Δ_t on the DMD will become smaller. In Fig. 5.8(b), we can see that when Δ_t alters, the DMD slope decreases no matter how we arrange the location of trench layer and design the refractive index of outer core.

We have known that adjusting a_1, Δ_1, r_1/a_1, Δ_d, and r_2/r_1 can help us find the required low DMD, low DMD slope, large A_{eff}. When these parameters are all set, we do not hope the both variables of trench structure — W/r_1 and Δ_t affect the results too much. Instead, W/r_1 and Δ_t can be used to control the bending loss of modes and the inter-core crosstalk. Therefore, we should deploy the trench layer far from the outer core, in other words, we need to increase r_2/r_1 as much as possible so that the change of W/r_1 and Δ_t will not influence the DMD and DMD slope a lot. However, we can conclude from Fig. 5.6 that if r_2/r_1 becomes larger than 1.6, the maximum absolute DMD over C+L bands will exceed 200 ps/km/nm, which is relative large value for DMD. Since MIMO system requires low DMD, we set 200 ps/km/nm to be the upper limit in this work. Hence, r_2/r_1 of 1.6 can be regarded as a relative optimum value, which can make TA-MSI-FMCs achieve relative low DMD over wide band and meanwhile have large tolerance of W/r_1 and Δ_t. More interestingly, when we set r_2/r_1 to 1.6, we can obtain two TA-MSI-FMCs with positive and negative DMD (−160 and +168 ps/km) whose absolute values are close to each other. This phenomenon implies that we can adopt DMD managed transmission line technique by using only one kind of Hetero-TA-FM-MCF and rotating one to splice different cores together to make the total DMD approach 0 ps/km over C+L bands.

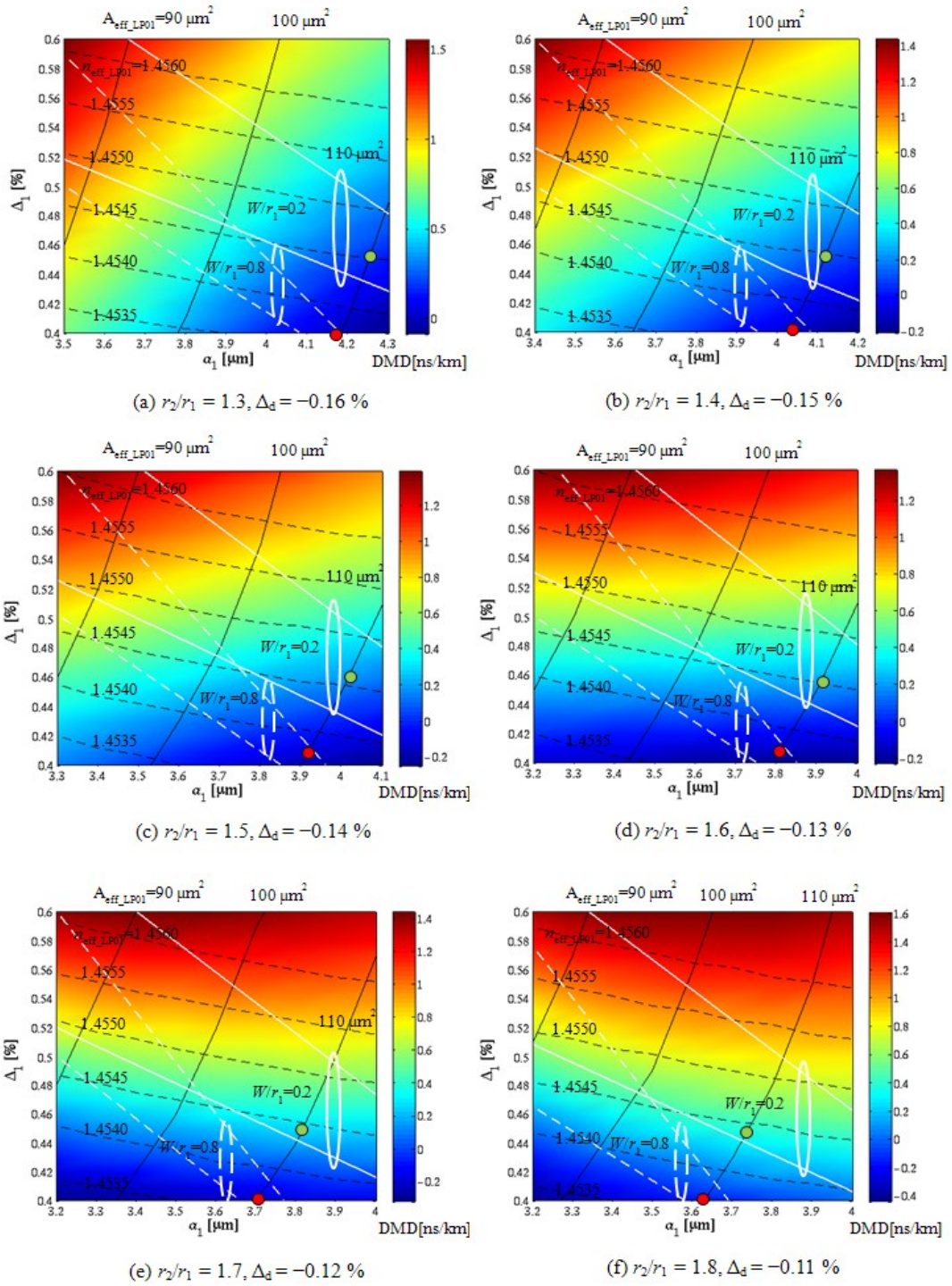

Fig. 5.5 DMD at λ of 1550 nm as function of a_1 and Δ_1 when r_1/a_1 = 2.0, W/r_1 = 1.0, and Δ_t = −0.7 %, where (a) r_2/r_1 = 1.3, Δ_d = −0.16 %, (b) r_2/r_1 = 1.4, Δ_d = −0.15 %, (c) r_2/r_1 = 1.5, Δ_d = −0.14 %, (d) r_2/r_1 = 1.6, Δ_d = −0.13 %, (e) r_2/r_1 = 1.7, Δ_d = −0.12 %, (f) r_2/r_1 = 1.8, Δ_d = −0.11%.

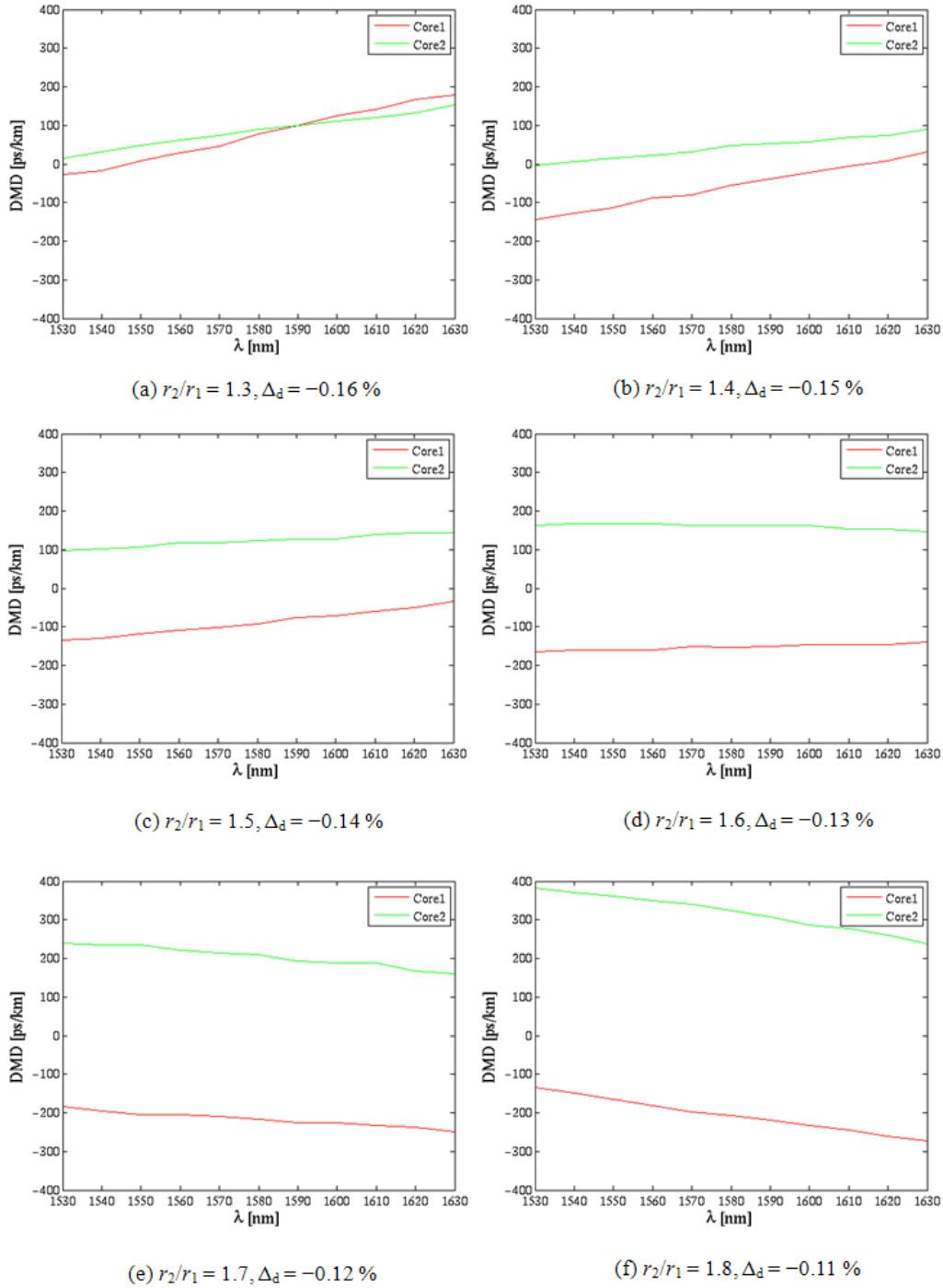

(a) $r_2/r_1 = 1.3, \Delta_d = -0.16$ %

(b) $r_2/r_1 = 1.4, \Delta_d = -0.15$ %

(c) $r_2/r_1 = 1.5, \Delta_d = -0.14$ %

(d) $r_2/r_1 = 1.6, \Delta_d = -0.13$ %

(e) $r_2/r_1 = 1.7, \Delta_d = -0.12$ %

(f) $r_2/r_1 = 1.8, \Delta_d = -0.11$ %

Fig. 5.6 Wavelength dependence of DMD for core 1 and core 2 when $r_1/a_1 = 2.0$, $\Delta_t = -0.7$ %, $W/r_1 = 0.8$ for core 1, and $W/r_1 = 0.2$ for core 2, where (a) $r_2/r_1 = 1.3$, $\Delta_d = -0.16$ %, (b) $r_2/r_1 = 1.4$, $\Delta_d = -0.15$ %, (c) $r_2/r_1 = 1.5$, $\Delta_d = -0.14$ %, (d) $r_2/r_1 = 1.6$, $\Delta_d = -0.13$ %, (e) $r_2/r_1 = 1.7$, $\Delta_d = -0.12$ %, (f) $r_2/r_1 = 1.8$, $\Delta_d = -0.11$%.

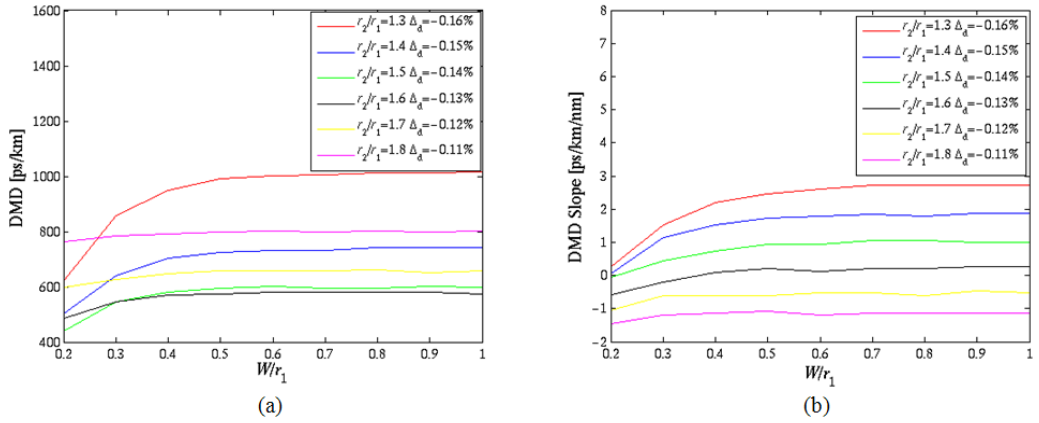

Fig. 5.7 (a) DMD dependence on W/r_1 and (b) DMD slope dependence on W/r_1 when a_1 = 3.6 μm, Δ_1 = 0.5 %, r_1/a_1 = 2.0, and Δ_t = −0.7 %.

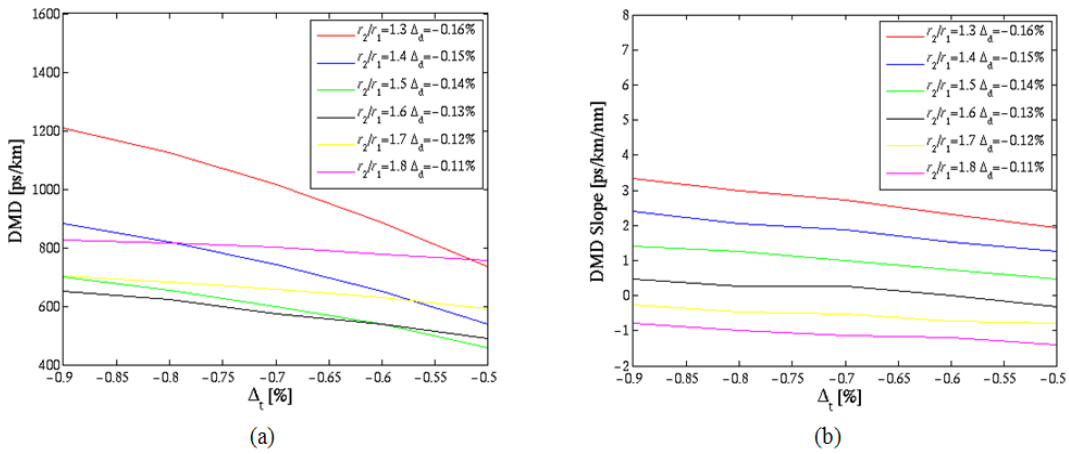

Fig. 5.8 (a) DMD dependence on Δ_t and (b) DMD slope dependence on Δ_t when a_1 = 3.6 μm, Δ_1 = 0.5 %, r_1/a_1 = 2.0, and W/r_1 = 1.0.

B. Layout of TA-MSI-FMCs in the fiber

According to the analyzation in above subsection, we can treat that r_2/r_1 of 1.6, Δ_d of −0.13 %, and r_1/a_1 of 2.0 as a relative optimum design scheme. Based on the design of these parameters, two kinds of TA-MSI-FMCs can be found which are shown in Fig. 5.4. The values of a_1, Δ_1, W/r_1, Δ_t and the characteristics of effective index (n_{eff}), mode field diameter (MFD), effective area (A_{eff}), dispersion parameter, DMD and *BL* of core 1 and core 2 are summarized in Tab. 5.1 and Tab. 5.2. The difference between effective index of inter-modes (Δn_{eff}') in core 1 and core 2 are 2.38×10^{-3} and 2.39×10^{-3}, which proves that mode-coupling phenomena in core 1 and core 2 can be limited because both Δn_{eff}' are larger than the critical value of 0.5×10^{-3} [9]. On the other hand, the difference between effective index of LP_{01} mode in core 1 and effective index of LP_{01} mode in core 2 (Δn_{eff_LP01}) is about 0.0008. The difference between effective index of LP_{11} mode in core 1 and effective index of LP_{11} mode in core 2 (Δn_{eff_LP11}) is also about 0.0008.

Table 5.1. The design parameters of core1 and core 2

	Unit	Core 1	Core 2
a_1	μm	3.81	3.92
Δ_1	%	0.406	0.458
W/r_1	-	0.8	0.2
Δ_t	%	−0.7	−0.7
r_1/a_1	-	2.0	2.0
Δ_d	%	−0.13	−0.13
r_2/r_1	-	1.6	1.6

Table 5.2. Characteristics of core1 and core 2

	Unit	Core 1	Core 2
LP_{01} n_{eff} at1550 nm	-	1.453753	1.454560
LP_{11} n_{eff} at1550 nm	-	1.451375	1.452169
LP_{01} MFD at1550 nm	μm	11.84	11.84
LP_{11} MFD at1550 nm	μm	16.92	16.68
LP_{01} A_{eff} at1550 nm	μm^2	110.12	110.12
LP_{11} A_{eff} at1550 nm	μm^2	224.85	218.58
LP_{01} Dispersion at1550 nm	ps/km/nm	21.64	19.88
LP_{11} Dispersion at1550 nm	ps/km/nm	20.90	21.60
DMD at 1550 nm	ps/km	−160.90	168.30
DMD slope at 1550 nm	ps/km/nm	0.27	−0.27
BL of LP_{11} at *R*=30 mm	dB/100 turns	0.21	0.07
BL of LP_{21} at *R*=140 mm	dB/m	1.81	62.89

As the proposals in our last works [21, 26], we arrange the TA-MSI-FMCs in a ring layout. If several layers of cores are set inside the fiber, the cut-off wavelengths of the interior cores tend to be longer than that of the exterior cores [25]. This is due to the tight confinements in the interior cores which are caused by the trench structure deployed around each core. Moreover, excessive crosstalk degradation will also happen in the inner cores [33].

In order to accommodate as many cores as possible in the fiber, we should shorten the core pitch (Λ) to the largest extent and meanwhile make sure the low crosstalk and small R_{pk}. The crosstalk of Hetero-MCF decreases immediately after bending radius (R) reaching a critical value R_{pk} and then it converges to a certain value no matter how R increases [14]. Therefore, we hope R_{pk} can be an extremely small value so that we can obtain a large non-phase-matching region with $R > R_{pk}$. In this non-phase-matching region, the bending extent doesn't impact the crosstalk any more, which can make us design a kind of bend-insensitive Hetero-TA-FM-MCF.

Fig. 5.9 shows inter-core LP_{01}-LP_{01} crosstalk ($XT_{01\text{-}01}$), LP_{01}-LP_{11} crosstalk ($XT_{01\text{-}11}$), LP_{11}-LP_{01} crosstalk ($XT_{11\text{-}01}$), and LP_{11}-LP_{11} crosstalk ($XT_{11\text{-}11}$) at λ=1550 nm, R = 500 mm, and propagation length (L) = 100 km as function of core pitch [48]. The reason why we set the R to be 500 mm is that this bending radius is much larger than the R_{pk}, which means that the crosstalk at R of 500-mm is the one in the bend-insensitive situation. In Fig. 5.9, we can find that $XT_{11\text{-}11}$ is the largest crosstalk of the three kinds of inter-core crosstalk. The $XT_{11\text{-}11}$ of less than −30 dB is realized when the core pitch becomes larger than about 37 μm. Fig 5.10 illustrates bending radius dependence of $XT_{11\text{-}11}$ at λ=1550 nm after 100-km propagation when Λ = 37 μm [48]. As shown in Fig. 5.10, in the case that Λ = 37 μm, R_{pk} is smaller than 15 cm which is a threshold value of R during the cabling process. It means that Λ of 37 μm can guarantee the bend-insensitive characteristics of the Hetero-TA-FM-MCF in the practical applications.

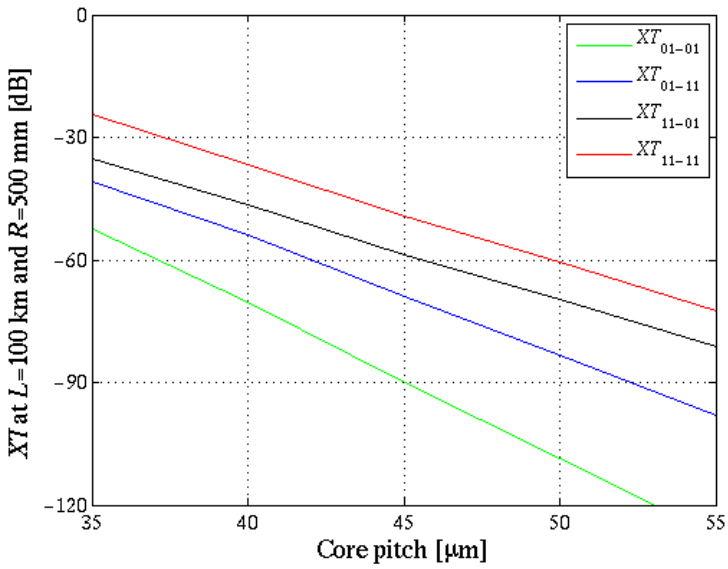

Fig. 5.9 Inter-core crosstalk at λ=1550 nm, R = 500, mm and L = 100 km as function of core pitch.

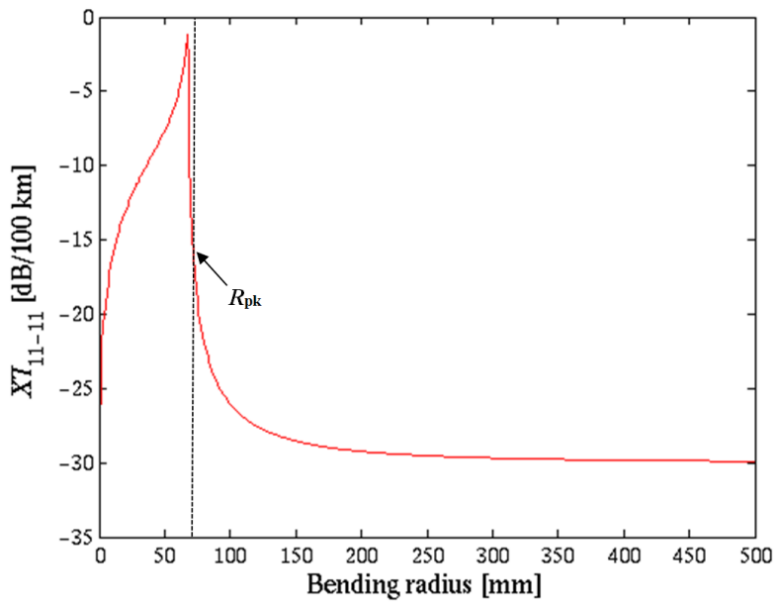

Fig. 5.10 Bending radius dependence of $XT_{11\text{-}11}$ at λ=1550 nm after 100-km propagation when Λ = 37 μm.

The cladding diameter (*CD*) can be determined by using the formula expressed as follows

$$CD = \frac{\Lambda}{\sin\left(\frac{\pi}{N_{\text{core}}}\right)} + 2OCT, \tag{5.2}$$

where N_{core} is the number of core and *OCT* is the radial distance between the center of the outer core and the cladding edge. In order to reduce the micro-bending loss, the *OCT* has different required minimum value corresponding to the different A_{eff}. If we expect the A_{eff} to reach 110 μm^2, the *OCT* needs to be at least 40 μm [15]. Additionally, if we want to decrease the failure probability of a fiber in order to guarantee the mechanical reliability, *CD* should not be larger than 225 μm [40]. The core pitch dependence of cladding diameter is shown as Fig. 5.11 [48]. From Fig. 5.11, we can find that when Λ equals 37 μm, N_{core} of 12 is the upper limit and in this case *CD* is about 223 μm.

According to the redefinition of core multiplicity factor (*CMF*) for FM-MCF [12], *CMF* for Hetero-FM-MCF can be proposed as follows:

$$CMF_{FM-MCF} = \frac{(N_{core}/2)\sum_{m}^{l} A_{eff-p-m} + (N_{core}/2)\sum_{m}^{l} A_{eff-q-m}}{(\pi/4)CD^2_{FM-MCF}}, \tag{5.3}$$

where $A_{\text{eff-}p\text{-}m}$ is effective area of *m*-th mode in core *p*, $A_{\text{eff-}q\text{-}m}$ is effective area of *m*-th mode in core *q*, *l* is the number of mode, $CD_{\text{FM-MCF}}$ is the cladding diameter of FM-MCF.

RCMF is a ratio between *CMF* of a FM-MCF and a standard single core single mode fiber with A_{eff} = 80 μm^2 at 1550 nm and *CD* = 125 μm, which is shown as

$$RCMF = CMF_{FM-MCF} \Big/ \frac{80}{(\pi/4)125^2}. \tag{5.4}$$

The *RCMF* of the two-LP mode Hetero-TA-12-core fiber (whose $A_{\text{eff-1}}$ of LP_{01} mode and LP_{11} mode are ~110 μm^2 and ~225 μm^2; $A_{\text{eff-2}}$ of LP_{01} mode and LP_{11} mode are ~110 μm^2 and ~219 μm^2) is 15.7. If we use the degenerated LP_{11} mode as two different special modes thinks to MIMO technology [49], the *RCMF* can be further enhanced to be 26.1 which exceeds the record value of 14.8 for a two-LP mode seven-core fiber [12]. Hence, we can design a kind of

two-LP mode Hetero-TA-MCF with N_{core} of 12, Λ of 37 μm, *OCT* of 40 μm, *CD* of 223 μm, *RCMF* of 15.7 for 24 special paths, and *RCMF* of 26.1 for 36 special paths.

Fig 5.12 shows the relationship between inter-core crosstalk (*XT*) and *RCMF* for the reported single-mode MCFs (SM-MCFs) [21, 26, 15, 40] and few-mode MCFs (FM-MCFs) [12]. In Fig. 5.12, the black circles represent the SM-MCFs with only LP_{01} mode, the blue triangles mean the FM-MCFs with LP_{01} mode and LP_{11} mode, the blue square stands for the FM-MCFs with LP_{01} mode, LP_{11a} mode and LP_{11b} mode. It is obvious that the Hetero-TA-FM-12-core fiber presented in this work [48] has the largest *RCMF*.

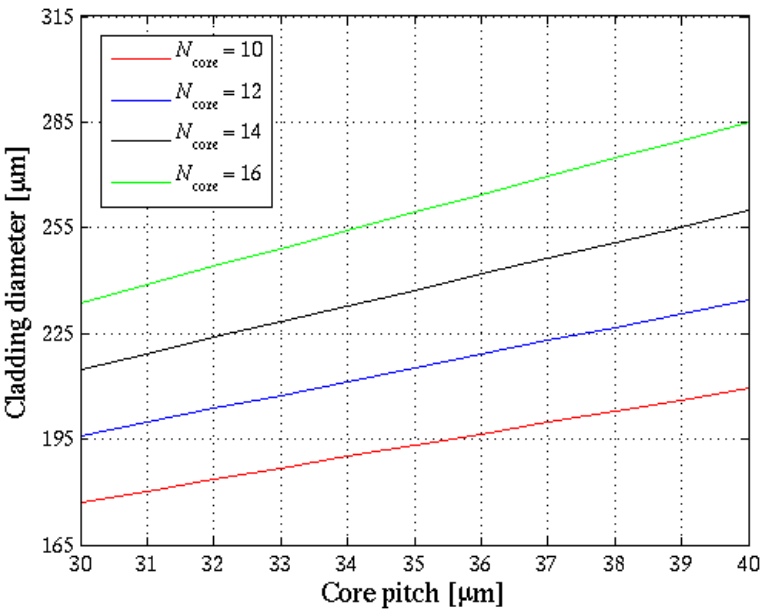

Fig. 5.11 Core pitch dependence of cladding diameter.

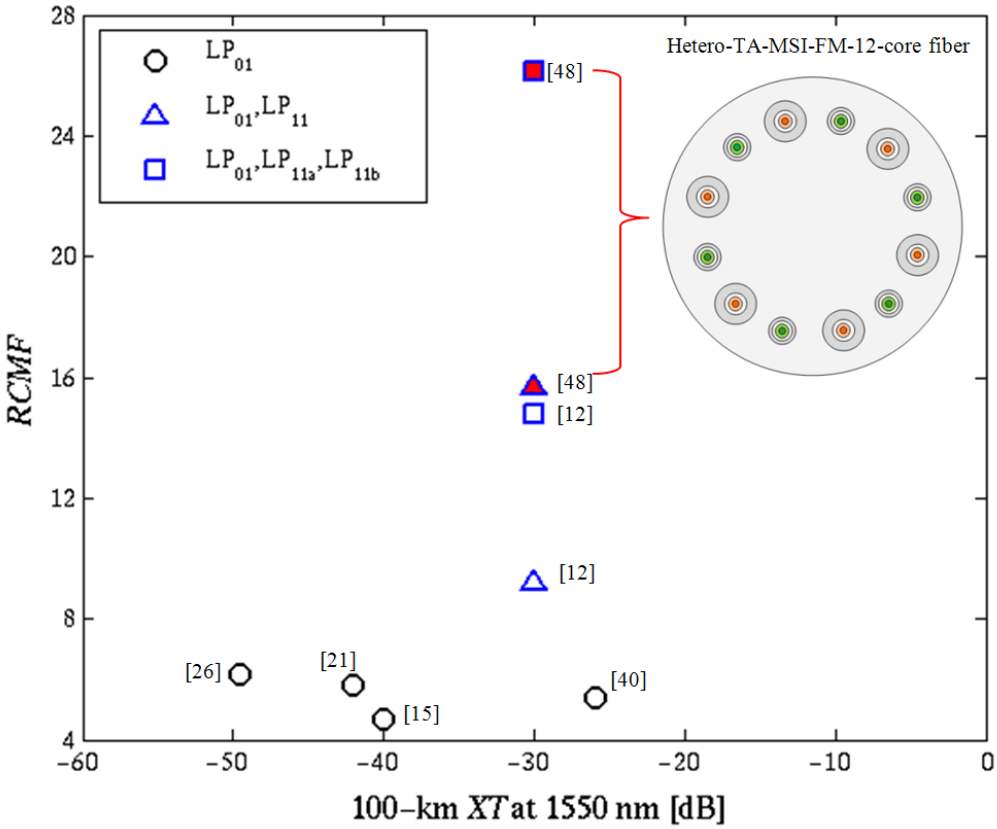

Fig. 5.12 The relationship between *XT* and *RCMF* for SM-MCFs and FM-MCFs.

5.4 Conclusion

To design a TA-MSI-FMC, there are seven parameters that determine the profile — a_1, Δ_1, r_1/a_1, Δ_d, r_2/r_1, W/r_1, and Δ_t. After analyzing how the r_2/r_1 and Δ_d affect the DMD and DMD slope for wavelength, we found that as r_2/r_1 changes, DMD and DMD slope will alter correspondingly and we can shift the absolute value of Δ_d to compensate the increment or decrement of the DMD and DMD slope. Furthermore, as r_2/r_1 increases, the maximum absolute DMD in two TA-MSI-FMCs over C+L bands is getting larger but the impact of W/r_1 and Δ_t on the DMD will become smaller. As a result, r_2/r_1 of 1.6 is regarded as a relative optimum design value since we should make sure not only the low DMD over wide band but also large tolerance of W/r_1 and Δ_t.

For the application of fiber, we propose two kinds of strategies. In the first strategy, we use a single heterogeneous few-mode multi-core fiber (Hetero-FM-MCF) to transmit the signal for the long-haul transmission because of the easy deployment. The DMD of each core is about |170| ps/km over C+L bands, which is not so small for MIMO processing, but the absolute DMD can be further decreased by increasing R_{pk} and decreasing A_{eff}. In the second strategy, we only use one kind of Hetero-FM-MCF and rotate one to splice different cores together to form DMD-managed transmission line so that the total DMD of almost 0 ps/km can be achieved over C+L bands.

After investigating the characteristics of crosstalk, R_{pk}, cladding diameter, and *RCMF*, we can design a kind of two-LP mode Hetero-TA-12-core fiber with *XT* of about –30 dB/100km at λ of 1550 nm as *R* becomes larger than 15 cm, *RCMF* of 15.7 for 24 special paths, and *RCMF* of 26.1 for 36 special paths. Actually, when the wavelength becomes larger, we can also obtain the low *XT* by scarifying R_{pk} and *RCMF* respectively.

Chapter 6 Conclusion

We have proposed an approximated analytical solution (AAS) to calculate mode-coupling coefficient (MCC) and it was proved that only when the $r_2/r_1 \geq 2.0$, the results based on the AAS close to the one obtained by finite element method (FEM). It implies that when the trench layer gets closer to the core, AAS is not as accurate as FEM.

We have presented the design method for the Hetero-TA-MCF. Subsequently we make compromises among crosstalk, A_{eff}, threshold value of bending radius (R_{pk}) [14] and relative core multiplicity factor (*RCMF*) [15] through the design process and then propose a relative optimal design scheme for the Hetero-TA-MCF. We proposed two kinds of relative optimized design schemes for Hetero-TA-14-core fiber. In the first case, we achieve a very small R_{pk} of about 31.7 mm, a large *RCMF* of 7.37, and a relative large center value of fabricated A_{eff} (F-A_{eff}) of around 90 μm^2 by sacrificing the crosstalk which is −28.4 dB/100 km. In the second case, the crosstalk is much lower which can reach about −50 dB/100 km, R_{pk} is 41.9 mm, *RCMF* is 6.16 and the center value of F-A_{eff} is about 85 μm^2.

What's more, we have presented the design method for the Hetero-TA-FM-MCF and then we investigate and analyze appropriate index profile for few-mode core that support two LP modes respectively. For the multi-step index profile, numerical simulations demonstrate that r_2/r_1 of 1.6 can be regarded as a relative optimum design value since we should make sure not only the low DMD over wide band but also large tolerance of W/r_1 and Δ_t. For the application of fiber, we proposed two kinds of strategies. After investigating the characteristics of crosstalk, R_{pk}, cladding diameter, and *RCMF*, we can design a kind of two-LP mode Hetero-TA-12-core fiber with *XT* of about –30 dB/100km at λ of 1550 nm as *R* becomes larger than 15 cm, *RCMF* of 15.7 for 24 special paths, and *RCMF* of 26.1 for 36 special paths. Actually, when the wavelength becomes longer, we can also obtain the low *XT* by scarifying R_{pk} and *RCMF* respectively.

Acknowledgement

It has been a great privilege to spend several years in the Graduate School of Information and Technology at Hokkaido University, and completing the Ph.D degree abroad is a big challenge and a good experience for me, which is a lovely memory in my life.

First of all, I want to express my deeply-felt thanks to my supervisor, Professor Kunimasa Saitoh, Division of Media and Network Technologies, Graduate School of Information Science and Technology, Hokkaido University, for his warm encouragement and thoughtful guidance.

Secondly, I want to express my gratitude to Professor Yoshikazu Miyanaga, Professor Toshio Nojima, and Professor Yasutaka Ogawa, Division of Media and Network Technologies, Graduate School of Information Science and Technology, Hokkaido University, for helpful suggestion and observation.

I am also grateful to Professor Masanori Koshiba, who has been retired form Division of Media and Network Technologies, Graduate School of Information Science and Technology, Hokkaido University last year. His rigorous research method and responsible instruction attitude impact me to a large extent so that I can threw myself into the research work actively every day.

I would like to thank all members in our laboratory for their fruitful discussion and illuminating suggestions.

Finally, I thank to all my friends and my family for their kindly support.

August 2014

Jiajing Tu

References

[1] T. Morioka, "New generation optical infrastructure technologies: "EXACT initiative" towards 2020 and beyond," in *Proceedings of 14th OptoElectronics and Communications Conference* (Institute of Electrical and Electronics Engineers, 2009), paper FT4.

[2] "NICT EXAT Initiative," *Journal of the ITU Association of Japan*, vol. 39, no. 5, pp. 3-25, May 2009 (in Japanese).

[3] K. Takenaga, S. Tanigawa, N. Guan, S. Matsuo, K. Saitoh, and M. Koshiba, "Reduction of crosstalk by quasi-homogeneous solid multi-core fiber," in *Optical Fiber Communication Conference*, OSA Technical Digest (CD) (Optical Society of America, 2010), paper OWK7.

[4] M. Koshiba, K. Saitoh, and Y. Kokubun, "Heterogeneous multi-core fibers: proposal and design principle," *IEICE Electronic Express*, vol. 6, no. 2, pp. 98-103, Jan. 2009.

[5] N. Hanzawa, K. Saitoh, T. Sakamoto, T. Matsui, S. Tomita, and M. Koshiba, "Demonstation of mode-division multiplexing transmission over 10 km two-mode fiber with mode coupler," in *Optical Fiber Communication Conference*, OSA Technical Digest (CD) (Optical Society of America, 2011), paper OWA4.

[6] M. Kasahara, K. Saitoh, T. Sakamoto, N. Hanzawa, T. Matsui, K. Tsujikawa, F. Uamamoto, and M. Koshiba, "Design of few-mode fibers for mode-division multiplexing transmission," *IEEE Photonics Journal.*, vol. 5, no. 6, article no. 7201207, Dec. 2013.

[7] J. Sakaguchi, B. J. Puttnam, W. Klaus, Y. Awaji, N. Wada, A. Kanno, T. Kawanishi, K. Imamura, H. Inaba, K. Mukasa, T. Sugizaki, T. Kobayashi, and M. Watanabe, "305 Tb/s space division multiplexed transmission using homogeneous 19-core fiber," *IEEE Journal of Lightwave Technology*, vol. 31 no. 4, pp. 554-562, Feb. 2013.

[8] H. Takara, A. Sano, T. Kobayashi, H. Kubota, H. Kawakami, A. Matsuura, Y. Miyamoto, Y. Abe, H. Ono, K. Shikama, Y. Goto, K. Tsujikawa, Y. Sasaki, I. Ishida, K. Takenaga, S. Matsuo, K. Saitoh, M. Koshiba, and T. Morioka, "1.01-Pb/s (12 SMD/222 WDM 456 Gb/s) crosstalk-managed transmission with 91.4–b/s/Hz aggregate spectral efficiency,"

in *European Conference and Exhibition on Optical Communication* (ECOC) (Optical Society of America, Washington, DC, 2012), paper Th.3 .C. 1.

[9] M. Bigot-Astruc, D. Boivin, and P. Sillard, "Design and fabrication of weakly-coupled few-modes fibers," in *IEEE photonics society summer topical meetings 2012*, paper TuC1.1.

[10] R. Maruyama, N. Kuwaki, S. Matuo. K. Sato, and M. Ohashi, "Mode dispersion compensating optical transmission line composed of two-mode optical fibers," in *Optical Fiber Communication Conference*, OSA Technical Digest (CD) (Optical Society of America, 2012), paper JW2A.13.

[11] T. Mori, T. Sakamoto, M. Wada, T. Yamamoto, and F. Yamamoto, "Low DMD four LP mode transmission fiber for wide-band WDM-MIMO system," in *Optical Fiber Communication Conference*, OSA Technical Digest (CD) (Optical Society of America, 2013), paper OTh3K.1.

[12] K. Takenaga, Y. Sasaki, N. Guan, M. Kasahara, K. Saitoh, and M. Koshiba, "Large effective-area few-mode multicore fiber", *IEEE Photonics Technology Letter*, vol. 24, no. 21, pp. 1941-1944, Nov. 2012.

[13] C. Xia, R. Amezcua-Correa, N. Bai, E. Antonio-Lopez, D. May-Arrioja, A. Schulzgen, M. Richardson, J. Linares, C. Montero, E. Mateo, X, Zhou, and G. Li, "Low-crosstalk few-mode multi-core fiber for high-mode-density space-division multiplexing," in *European Conference and Exhibition on Optical Communication* (ECOC) (Optical Society of America, Washington, DC, 2012), paper Mo.1.F.5.

[14] T. Hayashi, T. Taru, O. Shimakawa, T. Sasaki, and E. Sasaoka, "Design and fabrication of ultra-low crosstalk and low-loss multi-core fiber," *Optics Express*, vol. 19, no. 17, pp. 16576-16592, Aug. 2011.

[15] K. Takenaga, Y. Arakawa, Y. Sasaki, S. Tanigawa, S. Matsuo, K. Saitoh, and M. Koshiba, "A large effective area multi-core fiber with an optimized cladding thickness," *Optics Express*, vol. 19, no. 26, pp. B543-B550, Dec. 2011.

[16] K. Saitoh and M. Koshiba, "Full-vectorial imaginary-distance beam propagation method based on a finite element scheme: Application to photonic crystal fibers," *IEEE Journal of Quantum Electron*ics, vol. 38, no. 7, pp. 927-933, Jul. 2002.

[17] K. Okamoto, *Fundamentals of Optical Waveguides* (Corona Publishing, 1992), Chap. 4.

[18] D. Marcuse, *Light Transmission Optics* (Van Nostrand Reinhold, New York, 1972).

[19] A. Hardy, and W. Streifer, "Coupled-mode theory of parallel waveguides," *IEEE Journal of Lightwave Technology*, vol. 3, no. 5, pp. 1135-1146, Oct. 1985.

[20] E. Marcatili, "Improved coupled-mode equations for dielectric guides," *IEEE Journal of Lightwave Technology*, vol. OE-22, no.6, pp. 988-993, Jun. 1986.

[21] J. Tu, K. Saitoh, M. Koshiba, K. Takenaga, and S. Matsuo, "Design and analysis of large-effective-area heterogeneous trench-assisted multi-core fiber," *Optics Express*, vol. 20, no. 14, pp.15157-15170, Jul. 2012.

[22] H. D. Rudolph and E. G. Neuman, "Approximations for the eigenvalues of the fundamental mode of a step index glass fiber waveguide," *Nachrichtentechnische Zeitschrift*, vol. 29, pp. 328-329, Apr. 1976.

[23] A. W. Snyder and J. D. Love, *Optical Waveguide Theory* (Chapman & Hall, 1983), Chap. 37.

[24] F. Ye, J. Tu, K. Saitoh, H. Takara, and T. Morika, "Wavelength-dependent crosstalk in trench-assisted multi-core fibers," OptoElectronics and Communications Conference (OECC2014), Melbourne, Australia, paper TU5C-1.

[25] K. Takenaga, Y. Arakawa, S. Tanigawa, N. Guan, S. Matsuo, K. Saitoh, and M. Koshiba, "Reduction of crosstalk by trench-assisted multi-core fiber," in *Optical Fiber Communication Conference*, OSA Technical Digest (CD) (Optical Society of America, 2011), paper OWJ4.

[26] J. Tu, K. Saitoh, M. Koshiba, K. Takenaga, and S. Matsuo, "Optimized design method for bend-insensitive heterogeneous trench-assisted multi-core fiber with ultra-low crosstalk and high core density," *IEEE Journal of Lightwave Technology*, vol. 31, no. 15, pp. 2590-2598, Aug. 2013.

[27] D. Marcuse, *Theory of dielectric optical waveguides* (Academic Press, New York, 1974).

[28] A. W. Snyder, "Coupled-mode theory for optical fiber," *Journal of Optical Society of America*, vol. 62, no. 11, pp. 1267-1277, Nov. 1972.

[29] D. Marcuse, "Derivation of coupled power equations," *Bell System Technical Journal*, vol. 51, no. 1, pp. 229-237, Jan. 1972.

[30] M. Koshiba, K. Saitoh, K. Takenaga, and S. Matsuo, "Multi-core fiber design and analysis: coupled-mode theory and couple-power theory," *Optics Express*, vol. 19, no. 26, pp. B102-B111, Nov. 2011.

[31] S. Matsuo, K. Takenaga, Y. Arakawa, Y. Sasaki, S. Tanigawa, K. Saitoh, and M. Koshiba, "Crosstalk behavior of cores in multi-core fiber under bent condition," *IEICE Electronics Express*, vol. 8, no. 6, pp. 385-390, Mar. 2011.

[32] K. Takenaga, Y. Arakawa, S. Tanigawa, N. Guan, S. Matsuo, K. Saitoh, and M. Koshiba, "An investigation on crosstalk in multi-core fibers by introducing random fluctuation along longitudinal direction," *IEICE Transmissions on Communications*, vol. E94-B, no. 2, pp. 409-416, Feb. 2011.

[33] B. Zhu, T. F. Taunay, M. Fishteyn, X. Liu, S. Chandrasekhar, M. F. Yan, J. M. Fini, E. M. Monberg, and F. V. Dimarcello, "112-Tb/s Space-division multiplexed DWDM transmission with 14-b/s/Hz aggregate spectral efficiency over a 76.8-km seven-core fiber," *Optics Express*, vol. 19, no. 17, pp. 16665–16671, Aug. 2011.

[34] S. Matsuo, M. Ikeda, and K. Himeno, "Low-bending-loss and suppressed-splice-loss optical fibers for FTTH indoor wiring," in *European Conference and Exhibition on Optical Communication* (ECOC) (Optical Society of America, Washington, DC, 2004), paper ThI3.

[35] P. Sillard, S. Richard, L.-A. de Montmorillon, and M. Bigot-Astruc, "Micro-bend losses of trench-assisted single-mode fibers," in *Optical Fiber Communication Conference*, OSA Technical Digest (CD) (Optical Society of America, 2010), paper We.8.F.3.

[36] T. Matsui, K. Nakajima, and C. Fukai, "Applicability of photonic crystal fiber with uniform air-hole structure to high-speed and wide-band transmission over conventional telecommunication bands," *IEEE Journal of Lightwave Technology*, vol. 27, no. 23, pp. 5410-5416, Dec. 2009.

[37] M. Koshiba, K. Saitoh, K. Takenaga, and S. Matsuo, "Analytical expression of average power-coupling coefficients for estimating intercore crosstalk in multicore fibers," *IEEE Photonics Journal*, vol. 4, no. 5, pp.1987-1995, Oct. 2012.

[38] J. M. Fini, B. Zhu, T. F. Taunay, and M. F. Yan, "Statistics of crosstalk in bent multicore fibers," *Optics Express*, vol. 18, no. 14, pp. 15122-15129, Jul. 2010.

[39] K. Saitoh, M. Koshiba, K. Takenaga, and S. Matsuo, "Crosstalk and core density in uncoupled multicore fibers," *IEEE Photonics Technology Lett*ers, vol. 24, no. 21, pp. 1898-1901, Nov. 2012.

[40] S. Matsuo, K. Takenaga, Y. Arakawa, Y. Sasaki, S. Tanigawa, K. Saitoh, and M. Koshiba, "Large-effective-area ten-core fiber with cladding diameter of about 200 μm," *Optics Lett*ers, vol. 36, no. 23, pp. 4626-4628, Dec. 2011.

[41] S. Matsuo, Y. Sasaki, T. Akamatsu, I. Ishida, K. Takenaga, K. Okuyama, K. Saitoh, and M. Koshiba, "12-core fiber with one ring structure for extremely large capacity transmission," *Optics Express*, vol. 20, no. 27, pp. 28398-28408, Dec. 2012.

[42] T. Sakamoto, T. Mori, T. Yamamoto, and S. Tomita, "Differential mode delay managed transmission line for wide-band WDM-MIMO system", in *Optical Fiber Communication Conference*, OSA Technical Digest (CD) (Optical Society of America, 2012), paper OM2D.1.

[43] M. Li, E. Ip, and Y. Huang, "Large effective area FMF with low DMGD," in *IEEE photonics society summer topical meetings 2013*, paper MC3.4.

[44] K. Sato, R. Maruyama, N. Kuwaki, S. Matsuo, and M. Ohashi, "Optimized graded index two-mode optical fiber with low DMD, large A_{eff} and low bending loss," *Optics Express*, vol. 21, no. 14, pp. 16231-16238, Jul. 2013.

[45] T. Mori, T. Sakamoto, M. Wada, T. Yamamoto, and F. Yamamoto, "Low DMD four LP mode transmission fiber for wide-band WDM-MIMO system," in *Optical Fiber Communication Conference*, OSA Technical Digest (CD) (Optical Society of America, 2013), paper OTh3K.1.

[46] R. Maruyama, N. Kuwaki, S. Matsuo, K. Sato, and M. Ohashi, "DMD free transmission line composed of TMFs with large effective area for MIMO processing," in *European Conference and Exhibition on Optical Communication* (ECOC) (Optical Society of America, Washington, DC, 2012), paper Tu.1.F.2.

[47] T. Sakamoto, T. Mori, T. Yamamoto, and S. Tomita, "Differential mode delay managed transmission line for WDM-MIMO system using multi-step index fiber," *IEEE Journal of Lightwave Technology*, vol. 30, no 17, pp. 2783-2787, Sep. 2012.

[48] J. Tu, K. Saitoh, M. Koshiba, K. Takenaga, and S. Matsuo, "Heterogeneous trench-assisted few-mode multi-core fiber with low differential mode delay," *Optics Express*, vol.22, no. 4, pp.4329-4341, Feb. 2014.

[49] S. Randel, R. Ryf, A. H. Gnauck, M. A. Mestre, C. Schmidt, R. –J. Essiambre, P. J. Winzer, R. Delbue, P. Pupalaikis, A. Sureka, Y. Sun, X. Jiang, R. Lingle, and Jr, "Mode-multiplexed 6×20-GBd QPSK transmission over 1200-km DGD-compensated

few-mode fiber," in *Optical Fiber Communication Conference*, OSA Technical Digest (CD) (Optical Society of America, 2012), paper PDP5C.5.

List of Publications

Papers

[1] **Jiajing Tu**, Kunimasa Saitoh, Masanori Koshiba , Katsuhiro Takenaga, and Shoichiro Matsuo, "Design and analysis of large-effective-area heterogeneous trench-assisted multi-core fiber," *Optics Express*, vol. 20, no. 14, pp.15157-15170, Jul. 2012.

[2] **Jiajing Tu**, Kunimasa Saitoh, Masanori Koshiba, Katsuhiro Takenaga, and Shoichiro Matsuo, "Optimized design method for bend-insensitive heterogeneous trench-assisted multi-core fiber with ultra-low crosstalk and high core density," *Journal of Lightwave Technology*, vol. 31, no. 15, pp. 2590-2598, Aug. 2013.

[3] **Jiajing Tu**, Kunimasa Saitoh, Katsuhiro Takenaga, and Shoichiro Matsuo, "Heterogeneous trench-assisted few-mode multi-core fiber with low differential mode delay," *Optics Express*, vol.22, no. 4, pp.4329-4341, Feb. 2014.

International Conferences

[1] **Jiajing Tu**, Kunimasa Saitoh, Masanori Koshiba, Katsuhiro Takenaga, Shoichiro Matsuo, "Design and analysis of heterogeneous trench-assisted multi-core fiber under bending condition," Specialty Optical Fibers Conference (SOF), Stu2F.5, Colorado Spring, Colorado, USA, Jun.2012.

[2] **Jiajing Tu**, Kunimasa Saitoh, Masanori Koshiba, Katsuhiro Takenaga, Shoichiro Matsuo, "Large-effective-area heterogeneous trench-assisted twelve-core fiber under bending condition," OptoElectronics and Communications Conference (OECC), 5C1-3, Busan, Korea, Jul. 2012.

[3] **Jiajing Tu**, Kunimasa Saitoh, Masanori Koshiba, Katsuhiro Takenaga, and Shoichiro Matsuo, "Optimized design method for heterogeneous trench-assisted multi-core fiber," OptoElectronics and Communications Conference (OECC), MS1-5, Kyoto, Japan, Jul. 2013.

[4] Feihong Ye, **Jiajing Tu**, Kunimasa Saitoh, Hidehiko Takara, and Toshio Morika, "Wavelength-dependent crosstalk in trench-assisted multi-core fibers," OptoElectronics and Communications Conference (OECC 2014), accepted.

[5] Feihong Ye, **Jiajing Tu**, Kunimasa Saitoh, and Toshio Morika, "Theoretical investigation of inter-core crosstalk properties in homogeneous trench-assisted multi-core fibers," 2014 IEEE Summer Topical Meeting, accepted.

Domestic Conference

[1] **Jiajing Tu**, Kunimasa Saitoh, Masanori Koshiba, Katsuhiro Takenaga, Shoichiro Matsuo, "Low crosstalk heterogeneous multi-core fibers under bending condition," IEICE General Conference, Okayama, 20-23, Mar. 2012.

[2] **Jiajing Tu**, Kunimasa Saitoh, Masanori Koshiba, Katsuhiro Takenaga, Shoichiro Matsuo, "A bend-insensitive heterogeneous trench-assisted multi-core fiber with large effective area," Technical Committee on Optical Communication Systems Technical Meeting (OCS), Aug. 2012.